Journal of Marine Research, 62, 373–418, 2004

The effect of topography on the steady-state wind and buoyancy-driven Subtropical Gyre

by I. A. Walkington[1] and A. J. Willmott[1]

ABSTRACT

This paper studies the impact of topography and increased vertical resolution on steady-state wind and buoyancy-driven circulation in the Subtropical Gyre. Buoyancy driving is represented by mass exchange across the interface separating layers of constant density. The mass exchange in turn is parameterized in terms of the departure of a layer thickness from a reference value. A 2-layer ocean model is developed that incorporates topography that depends on the meridional co-ordinate, and the problem reduces to solving a first order partial differential equation governing the upper layer inverse planetary potential vorticity. Two distinct families of characteristic curves are required to span the entire subtropical gyre; an "interior family" emanating from the eastern boundary and a family lying in the northwestern corner that begin and end along the oceanic edge of the western boundary current. It is demonstrated that when the ocean shoals (deepens) poleward, the area of the recirculating gyre in the northwestern corner decreases (increases) in response to the increased (decreased) phase speed of long baroclinic Rossby waves. The model is applied to the subtropical North Atlantic gyre, using climatological Ekman pumping, zonally averaged topography and a realistic representation of the eastern boundary and the solutions are qualitatively compared with these from a general ocean circulation model. To address how increased vertical resolution modifies the recirculating gyre structure, solutions are calculated for a 3-layer flat bottom ocean model. The circulation in the top and bottom layers of this model are qualitatively similar to those in the 2-layer model. In the middle layer there is a recirculating anticyclonic gyre of extent similar to that in the 2-layer model. Outside this gyre is a second anticyclonic gyre of larger horizontal extent. The double-gyre structure in the middle layer is associated with the existence of two separatrices subdividing the layers into three regions. These curves separate two distinct families of characteristic curves each associated with the upper and lower layer inverse planetary potential vorticity equations.

1. Introduction

In a simple, but nevertheless thought provoking model of the Subtropical Gyre, Cushman-Roisin (1987; hereafter referred to as CR) proposes that within an anticyclonic recirculation region adjacent to the western boundary current, thermodynamics will play an important role in the circulation. This anticyclonic recirculation region, corresponding to the Sargasso Sea in the North Atlantic, is characterized by a narrow poleward western boundary current, with a broader return flow. By considering the potential vorticity budget

1. Department of Mathematics, Keele University, Keele, Staffordshire, ST5 5BG, United Kingdom. ***email: i.a.walkington@keele.ac.uk***

of a water parcel circulating around the Subtropical Gyre, CR demonstrates that the presence of a recirculation region in the northwestern corner of the domain, where intense cooling occurs, will permit fluid exiting the Gulf Stream (in the case of the North Atlantic) to re-enter the interior. CR also shows that an equivalent picture of the structure of the Subtropical Gyre is obtained from the viewpoint of ventilation theory.

More precisely, the way in which this wind and buoyancy-driven Subtropical Gyre operates is as follows. Downward Ekman pumping across the Subtropical Gyre drives fluid equatorward, in the eastern half of the domain, as dictated by classical Sverdrup dynamics. In the absence of either friction or thermodynamics operating in the western boundary current, parcels of fluid flowing poleward in the boundary layer will lead to an accumulation of waters in the upper layer of the exit region. As a consequence of this accumulation of waters, the thermocline is depressed, setting up a high pressure cell with a geostrophically balanced anticyclonic circulation.

How do the accumulated waters at the exit region of the boundary current, with a potential vorticity deficit, rejoin the interior? Lateral friction in the boundary current, leading to a source of positive relative vorticity, is invoked in classical wind-driven circulation models. Alternatively, CR proposes that water in the Sargasso Sea undergoes intense cooling, thereby increasing the potential vorticity and allowing the water parcels to rejoin the interior of the Subtropical Gyre. In this latter scenario the Sargasso Sea is characterized by an anticyclonic recirculation over which intense cooling operates and in which the upper layer potential vorticity is a minimum.

The purpose of this paper is to consider the impact of topography and increased vertical resolution on the structure of the recirculation region expounded by CR. Does the presence of topography force a dramatic change in the extent of the recirculating gyre? How does the horizontal extent of the recirculating gyre vary in each layer of a 3-layer model? We address these questions in the context of steady-state planetary geostrophic dynamics, in a 2- and 3-layer ocean model, forced by prescribed Ekman pumping, and with parameterized mass exchange between layers. Interfacial mass exchange parameterizes the impact of a surface heat flux on the ocean circulation. For example, if the water column is cooled then its density increases and it sinks into the deeper ocean moving from the upper layer to the lower layer. Therefore mass exchange between layers can be interpreted as a parameterization of the impact of a surface heat flux.

Following CR we do not *a priori* prescribe the distribution of mass exchange between the layers, but instead parameterize it in terms of the departure of a layer depth from an equilibrium value. A similar parameterization is adopted for the transfer of water out of the abyssal ocean into the thermocline in models of the buoyancy-driven planetary-scale abyssal circulation by Kawase (1988), Wright and Willmott (1992) and Willmott *et al.* (1996). In contrast, Luyten and Stommel (1986) prescribe the interfacial mass exchange, in what is otherwise a similar study to that of CR on the wind and buoyancy-driven Subtropical Gyre. The CR model is also generalized by Veronis (1988) to study the

circulation within the Subtropical and Subpolar Gyres on a spherical earth, rather than on a mid-latitude β-plane.

Spall (2001) examines a similar 2-layer model in an abyssal circulation context, but includes zonal topography. However, the parameter regimes analyzed in this paper make the use of Spall's method inappropriate. Also in the context of abyssal circulation Hautala and Riser (1989) developed a 3-layer wind and buoyancy driven model with arbitrary topography. The analysis of Hautala and Riser (1989) proceeds by decoupling the lower layer from the upper two layers. The upper two layers are then analyzed in isolation, yielding the 2-layer flat bottom solution, which is then substituted into the lower layer inverse planetary potential vorticity equation. The decoupling of the lower layer from the upper two layers removes the topographic effects from the upper layers, however this current paper shows the important role topography plays in the structure of the circulation in all layers.

Chen and Dewar (1993) develop a 3-layer model to examine intergyre communication. They show that each communication window corresponds to a Rossby repeller point, and the circulation patterns in each layer are confined to a decreasing area with increasing layer depth, a characteristic shared with the model developed in this paper. Following Rhines and Young (1982) this model assumes homogenized potential vorticity within closed streamlines, and therefore the circulation pattern within the recirculation region is not analyzed, in contrast to this paper. Nishino and Minobe (2000) use a 3-1/2-layer model to study the circulation patterns of mid-depth waters in the North Pacific. Again, the homogenization of potential vorticity within closed streamlines is assumed, and the model is solved under the assumption that the wind forcing dominates and that the buoyancy forcing is a small order correction term.

In this paper we adopt the quasi-geostrophic approximation of CR, thereby obtaining analytical solutions for a 2-layer ocean model in the presence of topography with linear slope orientated in the meridional direction, the equivalent nonlinear geostrophic 2-layer ocean model and a 3-layer quasi-geostrophic ocean model without topography. A method for determining the equivalent nonlinear geostrophic solutions for a 3-layer ocean is yet to be found. Thus, the quasi-geostrophic 3-layer solutions presented in this paper provide the only insight into the effects of increasing the vertical resolution on the structure of the recirculation region. The analytical solutions are particularly illuminating regarding the parameter sensitivity of the extent of the recirculation region in each layer. With one exception, solutions for the steady-state circulation in the presence of arbitrary 2-dimensional topography remain elusive. Salmon (2002) numerically solves for the steady-state 2-layer circulation above arbitrary topography in the case when: (a) there is no mass exchange between the layers; (b) inertial terms and linear bottom friction are retained in the momentum equations, the solutions thereby supporting a western boundary current in a meridional channel domain.

The plan of the paper is as follows. In Section 2 we formulate the 2-layer model and derive the nonlinear upper layer inverse planetary potential vorticity equation and the

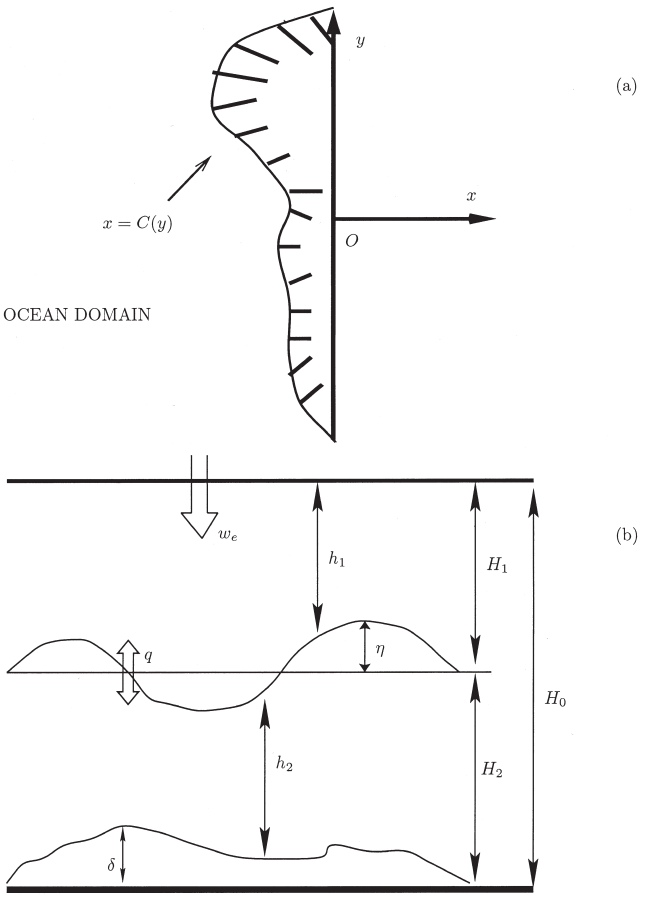

Figure 1. Schematic of; (a) the plan view of the ocean domain illustrating the eastern boundary and the coordinate system; (b) vertical section of the 2-layer model.

quasi-geostrophic approximation of the lower layer potential vorticity equation. Section 3 develops analytical solutions of the quasi-geostrophic potential vorticity equation, and the results are discussed in Section 4. In Section 5 results of the nonlinear model are discussed. The model described in Section 2 is then extended to 3 layers albeit in the absence of topography, and analytical solutions are again developed in Section 6. Results for the 3-layer model are presented in Section 7. The paper concludes in Section 8 with a summary and discussion.

2. 2-layer model formulation

Consider a 2-layer ocean model with latitude-dependent topography and an arbitrary eastern coastline (see Fig. 1(a)), provided that it is not multi-valued at any latitude in the

domain. Figure 1(b) shows a vertical zonal section of the model. With respect to a right-handed Cartesian co-ordinate frame with Ox directed eastward and Oy northward, the ocean occupies the domain $x < C(y)$. The governing equations for the interior steady-state geostrophic flow in a 2-layer model on a mid-latitude β-plane are

$$\mathbf{k} \times \mathbf{u_1} = \frac{-1}{\rho_0 f} \nabla p_s, \tag{1}$$

$$\nabla \cdot (\mathbf{u_1} h_1) = -w_e + q, \tag{2}$$

$$\mathbf{k} \times \mathbf{u_2} = \frac{-1}{f} \nabla \left(\frac{1}{\rho_0} p_s + g' \eta \right), \tag{3}$$

$$\nabla \cdot (\mathbf{u_2} h_2) = -q, \tag{4}$$

where $\mathbf{u_j} = (u_j, vj)$ is the horizontal velocity in layer j ($j = 1, 2$), $\mathbf{k}$ is a unit vector in the positive Oz direction, p_s is the pressure in the upper layer, $f = f_0 + \beta y$ is the Coriolis parameter, $\nabla \equiv (\partial_x, \partial_y)$ is the 2-dimensional gradient operator, w_e is the Ekman pumping at the base of the Ekman layer, q represents the fluid exchange between the layers, ρ_0 is a constant density, h_j is the depth of layer j, η is the displacement of the interface between the layers and $g' = g(\rho_2 - \rho_1)/\rho_2$ is reduced gravity. In the definition of g', layer j has constant density ρ_j. When w_e is negative, fluid is injected into the upper layer, and when q is negative fluid moves from the upper layer to the lower layer.

Following CR the effects of thermodynamics are parameterized by the inclusion of q in (2) and (4). The presence of topography is explicitly included in the definition of h_2, since

$$h_1 + h_2 = H_0 - \delta(y), \tag{5}$$

where $z = -H_0$ is the reference level from which the height of the topography, $\delta(y)$, is measured (see Fig. 1). Upon eliminating $\mathbf{u_j}$ between (1) and (4) we obtain

$$J\left(\frac{1}{\rho_0} p_s, \frac{h_1}{f} \right) = -w_e + q, \tag{6}$$

$$J\left(\frac{1}{\rho_0} p_s + g' \eta, \frac{h_2}{f} \right) = -q, \tag{7}$$

where J is the Jacobian operator defined as

$$J(A, B) = \frac{\partial A}{\partial x} \frac{\partial B}{\partial y} - \frac{\partial A}{\partial y} \frac{\partial B}{\partial x}.$$

The generalized Sverdrup balance is obtained by adding (6) and (7) and then zonally integrating from the eastern boundary at $x = C(y)$:

$$\frac{1}{\rho_0} p_s + \frac{g'}{\mu} \left(\frac{\beta h_2}{2f} + \delta_y \right) h_2 = \Psi + \Gamma. \tag{8}$$

In (8)

$$\Psi(x, y) = \frac{-f}{\mu}\int_{x}^{C(y)} w_e(s, y)ds,$$

$$\Gamma(y) = \frac{1}{\rho_0}p_s^e + \frac{g'}{\mu}\left(\frac{\beta h_2^e}{2f} + \delta_y\right)h_2^e,$$

$$\mu(y) = \delta_y + \frac{\beta}{f}(H_0 - \delta).$$

The superscript e appearing in Γ denotes the value of the variable at the eastern boundary. Eq. (8) relates the pressure, p_s to the layer depths. Eliminating p_s in (6) using (8), we obtain the governing equation for the lower layer inverse planetary potential vorticity, h_2/f, namely

$$\left[-\Psi_y - \frac{\beta^2 g' h_2}{f^2\mu}(H_0 - h_2 - \delta) - \frac{\beta g'\delta_y}{f\mu}(H_0 - h_2 - \delta) - \frac{\beta g'\delta_{yy}}{2f\mu^2}(h_2^2 - (h_2^e)^2 + 2(H_0 - \delta)(h_2^e - h_2))\right]\left(\frac{h_2}{f}\right)_x + \Psi_x\left(\frac{h_2}{f}\right)_y = -q. \tag{9}$$

To make further progress we must specify w_e and introduce a parameterization for q. Following CR

$$w_e = -w_0\left(1 - \frac{y^2}{l^2}\right), \tag{10}$$

where w_0 is the maximum amplitude of the Ekman pumping velocity and $2l$ is the meridional extent of the domain. The form of q can either be prescribed, following Luyten and Stommel (1986), or it may be parameterized as $q = -k(h_1 - \bar{h})$, following CR. In this parameterization, $\bar{h}$ is a constant relaxation depth. This parameterization has the advantage that the distribution of q is internally calculated as part of the problem, and will be used hereafter in this paper.

Adopting this parameterization of q the lower layer inverse planetary potential vorticity equation (9) is a first order quasi-linear partial differential equation. Subsequent analysis can follow two paths. Numerical solutions of (9) can be calculated using the method characteristics, an approach that is adopted in Section 5. Alternatively, the approach followed in Sections 3 and 4 is to analyze the quasi-geostrophic approximation of (9), the advantage being that, analytical progress can be made in obtaining solutions for the gyre structure. In these solutions it becomes transparent how bottom topography, the parameterization of q and the strength of the Ekman pumping influence the gyre structure, particularly in the interesting northwest corner of the domain where a recirculating gyre (identifiable as the Sargasso Sea region, in the case of the N. Atlantic) naturally emerges.

The quasi-geostrophic approximation is valid for the regime of weak Ekman pumping and small amplitude interfacial displacement. Upon writing $h_2 = H_2 + \eta - \delta$, and assuming that $(\beta y/f_0)$ and $(\eta/(H_2 - \delta))$ are both small to the same degree, and that $|\delta_y| = O(\beta H_2/f_0)$, (9) reduces to the linear first order partial differential equation

$$\left[\frac{\Psi_y}{f_0} + \frac{\beta g'}{f_0^2} H_1 - \frac{\beta^2 g'}{f_0^3 \mu} H_1^2\right]\eta_x - \frac{\Psi_x}{f_0}\eta_y = -w_e\left(1 - \frac{\beta H_1}{f_0 \mu}\right) + k\eta - k(H_1 - \bar{h}). \quad (11)$$

The generalized Sverdrup balance (8) becomes in this quasi-geostrophic limit,

$$\frac{1}{\rho_0} p_s + g'\eta - \frac{\beta g' H_1}{f_0 \mu}\eta + \frac{g'(H_2 - \delta)}{\mu}\left[\delta_y + \frac{\beta}{2f_0}(H_2 - \delta)\right] = \Psi + \Gamma, \quad (12)$$

where

$$\Psi(x, y) = \frac{-f_0}{\mu}\int_x^0 w_e(s, y)ds, \quad (13)$$

$$\Gamma(y) = \frac{1}{\rho_0} p_s^e + g'\eta^e - \frac{\beta g' H_1}{f_0 \mu}\eta^e + \frac{g'(H_2 - \delta)}{\mu}\left[\delta_y + \frac{\beta}{2f_0}(H_2 - \delta)\right], \quad (14)$$

$$\mu(y) = \delta_y + \frac{\beta}{f_0}(H_0 - \delta). \quad (15)$$

In the quasi-geostrophic models the eastern boundary is assumed to be a line of constant longitude given by $C(y) = 0$. The inclusion of a more realistic eastern boundary introduces no new physical processes, rather it only increases the algebraic complexity of the solutions. A more realistic form for $C(y)$ is introduced in Section 5. In Section 3 we develop analytical solutions of (11) driven by the Ekman pumping (10) numerically using the Backward Differentiation Formulae (NAG, version 20, routine d02ejf) subject to no-normal flow on the eastern boundary. Explicitly the boundary conditions are

$$h_1(C(y), y) = h_1^e \text{ (a constant)}, \quad (16)$$

$$\frac{h_1(-L, y_1)}{f(y_1)} = \frac{h_1(-L, y_2)}{f(y_2)}, \quad (17)$$

where y_1 and y_2 are the start and end latitudes of a characteristic that begins and ends at the oceanic edge of the western boundary current. The solutions are discussed in Section 5.

3. Solution of the quasi-geostrophic 2-layer problem

a. Topography of the form δ(y)

To obtain analytical solutions of (11) it is convenient to re-cast this equation in the form

$$J(\phi, \eta) = w_e\left(1 - \frac{\beta H_1}{f_0 \mu}\right) - k\eta + k(H_1 - \bar{h}) \quad (18)$$

where

$$\phi(x, y) = \frac{\Psi}{f_0} + \frac{\beta g' H_1}{f_0^2} y - \frac{\beta^2 g' H_1^2}{f_0^3} \int \frac{dy}{\delta_y + \frac{\beta}{f_0}(H_0 - \delta)}. \tag{19}$$

Upon regarding η as a function of ϕ and y, (18) becomes

$$\eta_y + \frac{k\mu}{w_e}\eta = \mu - \frac{\beta H_1}{f_0} + \frac{k\mu}{w_e}(H_1 - \bar{h}). \tag{20}$$

The general solution of (20) is given by

$$\eta = \bar{\eta}(\phi)e^{-I(y)} + G(y)e^{-I(y)} + (H_1 - \bar{h}) \tag{21}$$

where $\bar{\eta}(\phi)$ is an arbitrary function and

$$G(y) = \int \left(\mu - \frac{\beta H_1}{f_0}\right) e^{I(y)} dy,$$

$$I(y) = \int \frac{k\mu}{w_e} dy.$$

To complete the solutions for η, an appropriate boundary condition must be imposed to determine $\bar{\eta}$. The domain of interest is the interior of the subtropical gyre (i.e. excluding the western boundary current) bounded to the east by a meridional vertical coastal wall as $x = 0$. This domain is spanned by two distinct families of characteristics, in a manner analogous to the CR model. One family of characteristic curves emanates from the eastern boundary, where we impose the condition of no-normal flow in each layer. The second family of characteristic curves spans the northwest corner of the domain. These curves begin and end along the oceanic edge of the western boundary current. The question that naturally arises is what is the boundary condition that is required for integration along these curves? CR proposes that the upper layer potential vorticity is conserved along streamlines within the western boundary layer because the flow is rapid giving little opportunity for the nonconservative processes (i.e. w_e and q) to operate. Thus, CR imposes the constraint that the upper layer potential vorticity at the start and end points of the characteristic curves in the northwest corner region is identical. This assumption will also be adopted in this model. Alternatively, we might speculate that high mixing rates exist at the outflow region of the western boundary current due to eddies, thereby homogenizing potential vorticity. The impact of eddy induced mixing in the outflow region of the western boundary current is considered by Scott and Willmott (2002) in a study of meridional heat transport in the Subtropical Gyre using a thermodynamic reduced gravity model. Scott and Willmott

(2002) assume that enthalpy is uniformly mixed, thereby forming the basis of a parameterization for the heat transport within the boundary current.

At the eastern boundary, $x = 0$, the condition of no-normal flow is satisfied provided $\eta = \eta^e$, a constant. Using (21) we then obtain

$$\bar{\eta}(\phi) = (\eta^e - (H_1 - \bar{h}))e^{I(\bar{y})} - G(\bar{y}), \tag{22}$$

where $\bar{y}$ is the solution of $\phi(x, y) = \phi(0, \bar{y})$, the initial latitude of each characteristic at the eastern boundary.

For characteristics that begin and end along the oceanic edge of the western boundary current, $x = -L$, the potential vorticity constraint is equivalent to requiring

$$\eta(-L, y_1) - \eta(-L, y_2) = \frac{\beta H_1}{f_0}(y_2 - y_1), \tag{23}$$

where y_1 and y_2 are the start and end points of the characteristic, respectively. Using (23) we can show that

$$\bar{\eta}(\phi) = \frac{\left[\dfrac{\beta H_1}{f_0}(y_2 - y_1) + G(y_2)e^{-I(y_2)} - G(y_1)e^{-I(y_1)}\right]}{\exp(-I(y_1)) - \exp(-I(y_2))}. \tag{24}$$

In general, analytical forms for $G(y)$, and hence $\bar{\eta}(\phi)$, are available for limited, but nevertheless oceanographically relevant, classes of bottom topography δ.

b. Flat bottom limit

In the absence of topography, $\delta \equiv 0$, and (19) reduces to

$$\phi(x, y) = \frac{\Psi}{f_0} + \beta R^2 y, \tag{25}$$

where $R^2 = g' H_1 H_2/(f_0^2 H_0)$ is the internal Rossby radius of deformation. With the Ekman pumping velocity (10) and a constant value for k in the parameterization of q, the integrals in (21) exhibit logarithmic singularities at $y = \pm l$, as noted by CR. Following CR, these singularities are avoided by assuming that k varies with latitude according to $k = K(1 + y/l)$, where K is a constant. Clearly there is a high degree of flexibility in parameterizing the diabatic processes, and this choice of k is no better, or worse, than a constant value. Secondly, this non-uniform value of k does not add, or remove, any physical processes. Thirdly, since $y = -l$ is a characteristic, the zero of k at $y = -l$ does not impact on the solution in the domain of interest. Using this parameterization for k we obtain

$$I(y) = \alpha ln(l - y), \tag{26}$$

$$G(y) = -\frac{\beta(H_0 - H_1)}{f_0(\alpha + 1)}(l - y)^{\alpha+1}, \tag{27}$$

where

$$\alpha = \frac{\beta H_0 K l}{f_0 w_0}. \tag{28}$$

It will be seen that the magnitude of α controls the structure of the recirculating gyre in the northwest corner of the domain.

The general solution for the flat bottom model is

$$\eta = \bar{\eta}(\phi)(l - y)^{-\alpha} - \frac{\beta(H_0 - H_1)}{f_0(\alpha + 1)}(l - y) + H_1 - \bar{h}. \tag{29}$$

Now we can evaluate the unknown function $\bar{\eta}(\phi)$, for the two distinct families of characteristics, and thus the solution in the two distinct regions. For the characteristics emanating from the eastern boundary we find that

$$\begin{aligned}\eta = \eta^e\left[1 + \frac{f_0 w_0 x}{\beta^2 R^2 H_0 l^2}(l + y)\right]^{\alpha} - (H_1 - \bar{h})\left(1 + \frac{f_0 w_0 x}{\beta^2 R^2 H_0 l^2}(l + y)\right)^{\alpha} \\ - \frac{\beta(H_0 - H_1)}{f_0(\alpha + 1)}(l - y)\left[1 - \left(1 + \frac{f_0 w_0 x}{\beta^2 R^2 H_0 l^2}(l + y)\right)^{\alpha+1}\right].\end{aligned} \tag{30}$$

For the characteristics that begin and end along the oceanic edge of the western boundary current we obtain

$$\begin{aligned}\eta = (H_1 - \bar{h}) - \frac{\beta H_0\left(1 - \dfrac{H_1}{H_0}\right)}{f_0(\alpha + 1)}(l - y) \\ - \frac{\beta H_1\left(\alpha + \dfrac{H_0}{H_1}\right)(y_2 - y_1)}{f_0(\alpha + 1)[(l - y_2)^{\alpha} - (l - y_1)^{\alpha}]}\left[-\frac{x(l + y)}{L} - \frac{\beta^2 R^2 H_0 l^2}{f_0 w_0 L}\right]^{\alpha},\end{aligned} \tag{31}$$

where y_1 and y_2 are the latitudes of the characteristic at the points where it meets the oceanic edge of the western boundary current. These latitudes are the solutions to the equation

$$\phi(\hat{x}, \hat{y}) = \frac{f_0 w_0 L}{\beta H_0}\left(1 - \frac{y_i^2}{l^2}\right) + \beta R^2 y_i. \tag{32}$$

where $i = 1, 2$ specifies which solution, and $\hat{x}$, $\hat{y}$ is the position being considered in the domain.

c. Linear sloping bottom

In the presence of linear sloping topography of the form $\delta(y) = ay$, (19) becomes

$$\phi(x, y) = \frac{\Psi}{f_0} + \frac{\beta g' H_1}{f_0^2}\, y + \frac{\beta g' H_1^2}{f_0^2 a} \ln\left(\frac{f_0 a}{\beta} + H_0 - ay\right), \tag{33}$$

using the nonuniform parameterization for k introduced in Section 3b, and

$$I(y) = \alpha\left(\left[1 + \frac{a}{H_0}\left(\frac{f_0}{\beta} - l\right)\right]\ln(l - y) - \frac{ay}{H_0}\right). \tag{34}$$

It is clear that (34) reduces to the flat bottom solution (26) when $a = 0$. It will be demonstrated that as in the flat bottom case, the magnitude of α controls the structure of the recirculating gyre. However, the explicit dependence of I on the topography shows that the latter will exert influence on the recirculating gyre structure also.

For a linear sloping bottom $G(y)$ can only be written in the integral form

$$G(y) = \int \left(a + \frac{\beta(H_0 - H_1)}{f_0} - \frac{\beta a}{f_0}\, y\right)(l - y)^{\gamma} e^{-\nu y} dy \tag{35}$$

where

$$\gamma = \frac{\beta K l}{w_0 f_0}\left(H_0 + a\left(\frac{f_0}{\beta} - l\right)\right), \tag{36}$$

$$\nu = \frac{\beta K l a}{w_0 f_0}. \tag{37}$$

4. Results of the quasi-geostrophic model

Consider first the impact on the recirculating gyre of introducing meridionally varying topography. Figure 2 shows a contour plot of the characteristics of (18) spanning the entire subtropical gyre, without topography. The parameter values employed in Figure 2 are listed in Table 1. Two distinct families of characteristic curves span the entire domain. Associated with these two families of characteristics is a separatrix. The point where the separatrix intersects the northern open boundary is called the Rossby Repeller Point, denoted by R in Figure 2. At R the speed of the long, non-dispersive baroclinic Rossby waves is identical to the zonal depth integrated wind-driven velocity. The center of the recirculating gyre in the northwest corner of the domain is marked as C in Figure 2. The impact of the topography introduced in Section 3c on the location of the points R and C can be determined analytically.

At $R \equiv (x_R, l)$, a stagnation point, we note that

$$\phi_x = 0 = \phi_y,$$

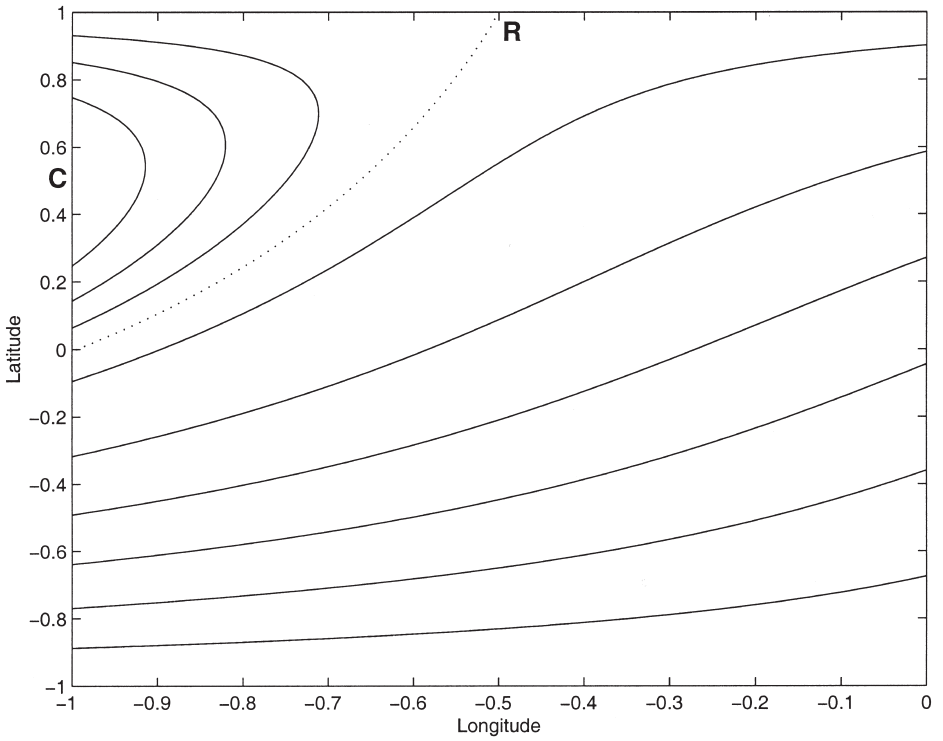

Figure 2. Plot of characteristic curves for 2-layer model without topography.

which upon using (33) yields

$$x_R = -\frac{\beta^2 g' H_1 H_2 l}{2f_0^3 w_0} - \frac{\beta g' H_1 l}{2f_0^2 w_0}\left(\delta_y(l) - \frac{\beta\delta(l)}{f_0}\right). \tag{38}$$

Consider the impact of linear topography, $\delta(y) = ay$, on x_R. In this case

$$x_R = -\frac{\beta^2 g' H_1 H_2 l}{2f_0^3 w_0} - \frac{\beta g' H_1 l a}{2f_0^2 w_0}\left(1 - \frac{\beta l}{f_0}\right). \tag{39}$$

Table 1. Table of parameter values used in the 2-layer and 3-layer model results.

$f_0 = 7.3 \times 10^{-5}$ s^{-1}	$\beta = 2 \times 10^{-11}$ m^{-1} s^{-1}
$l = 1.4 \times 10^6$ m	$L = 5.5 \times 10^6$ m
$H_0 = 4 \times 10^3$ m	$H_1 = 200$ m
$\bar{h} = 200$ m	$w_0 = 1 \times 10^{-6}$ m s^{-1}
$g' = 5 \times 10^{-3}$ m s^{-2}	$K = 5 \times 10^{-10}$
deepening to north $a = 2 \times 10^{-4}$	shoaling to north $a = -2 \times 10^{-4}$

When $a > 0$, corresponding to the ocean shoaling to the north, we see from (39) that x_R is displaced westward from the flat bottom value. We can understand this result by considering the impact of topography on long baroclinic Rossby waves. When the ocean depth shoals to the north, the topographic beta effect reinforces the planetary β-effect, leading to an increase in the speed of the long baroclinic Rossby waves. At R, the eastward depth integrated wind-driven velocity is equal and opposite to the long Rossby wave speed. An increase in the latter displaces R westward. Conversely, when $a < 0$, corresponds to the ocean depth increasing to the north, the speed of the long Rossby waves decreases and R is displaced eastward from the flat bottom location. In principle R could be displaced to the eastern boundary ($x = 0$), when the speed of the long topographic Rossby waves is zero, due to the self-cancellation of the ambient planetary and topographic vorticity gradients. From (39) it is readily seen that when $x_R = 0$

$$a = -\frac{\beta(H_0 - H_1)}{f_0 - \beta l}. \tag{40}$$

Evaluating (40) using the parameter values listed in Table 1, we find that a typical value for a is -1.69×10^{-3}. On the other hand, point R will lie on the oceanic edge of the western boundary current ($x = -L$) when

$$a = \frac{2f_0^3 w_0 L}{\beta g' H_1 l(f_0 - \beta l)} - \frac{\beta(H_0 - H_1)}{f_0 - \beta l}. \tag{41}$$

In this case evaluation of (41) shows that a typical value of a is 1.71×10^{-3}.

Now consider the impact of the topography $\delta(y) = ay$ on the location of the recirculating gyre center C. At $C = (-L, y_c)$, the following conditions are satisfied

$$\frac{\partial}{\partial y}(PV) = 0, \tag{42a}$$

$$\phi_y = 0. \tag{42b}$$

Condition (42a) was proposed by CR, based on the assumption that the potential vorticity is identical at the exit and entrance points where a given streamline intersects the oceanic edge of the western boundary current. Thus, at C the potential vorticity must be an extremum. This provides the interfacial displacement, η, at C given the latitude. Condition (42b) is simply a statement of the vanishing of the zonal velocity at C. Using (33), we find that (42b) yields

$$\frac{\Psi_y}{f_0} + \frac{\beta g' H_1}{f_0^2} - \frac{\beta^2 g' H_1^2}{f_0^3 \mu} = 0 \qquad \text{at } C. \tag{43}$$

Using (13) we then find from (43) that y_c satisfies the quadratic

$$Ay_c^2 + By_c + C = 0 \tag{44}$$

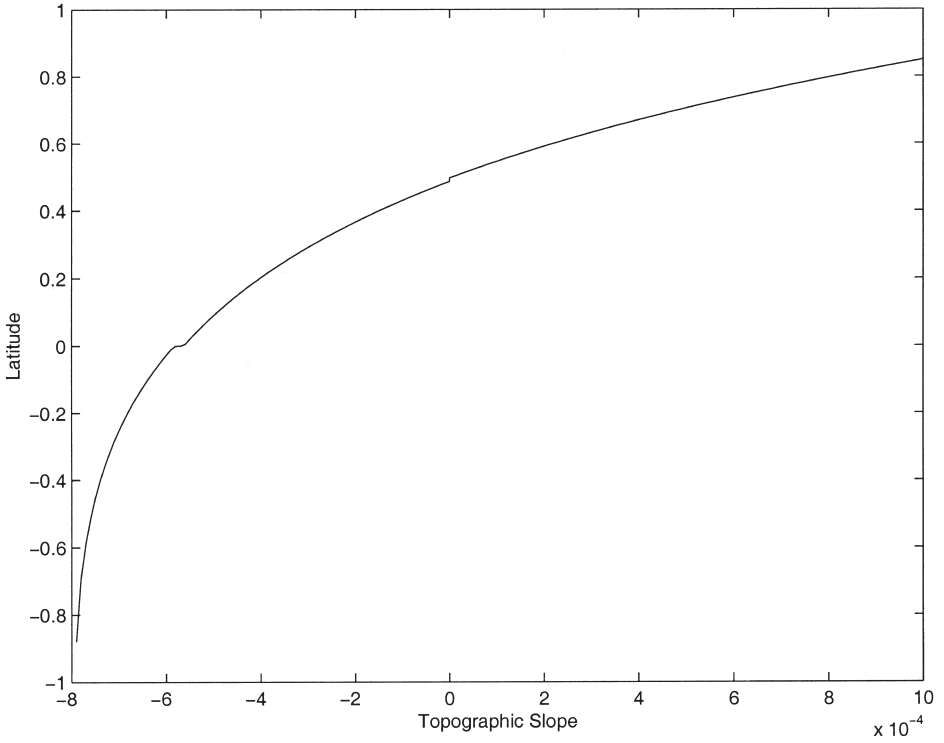

Figure 3. Plot of gyre center latitude for varying linear bottom slope.

where

$$A \equiv \frac{\beta L w_0 a}{l^2} + \frac{\beta^3 g' H_1 a^2}{f_0^3}$$

$$B \equiv -\frac{2\beta L w_0 H_0}{l^2} - \frac{2 f_0 L w_0 a}{l^2} - \frac{\beta^3 g' H_1 (H_0 + H_2) a}{f_0^3} - \frac{2\beta^2 g' H_1 a^2}{f_0^2}$$

$$C \equiv \beta L w_0 a + \frac{\beta^3 g' H_1 H_2 H_0}{f_0^3} + \frac{\beta^2 g' H_1 H_2 a}{f_0^2} + \frac{\beta g' H_1 a}{f_0} + \frac{\beta^2 g' H_0 H_1 a}{f_0^2}.$$

Upon setting $a = 0$ the solution for the latitude of the recirculating gyre center in the absence of topography is recovered, namely

$$y_c = \frac{\beta^2 g' H_1 H_2 l^2}{2 f_0^3 w_0 L}. \tag{45}$$

Figure 3 shows a plot of y_c against linear bottom slope a. For an ocean with depth shoaling to the north ($a > 0$) the recirculating gyre center moves poleward, and vice versa for the

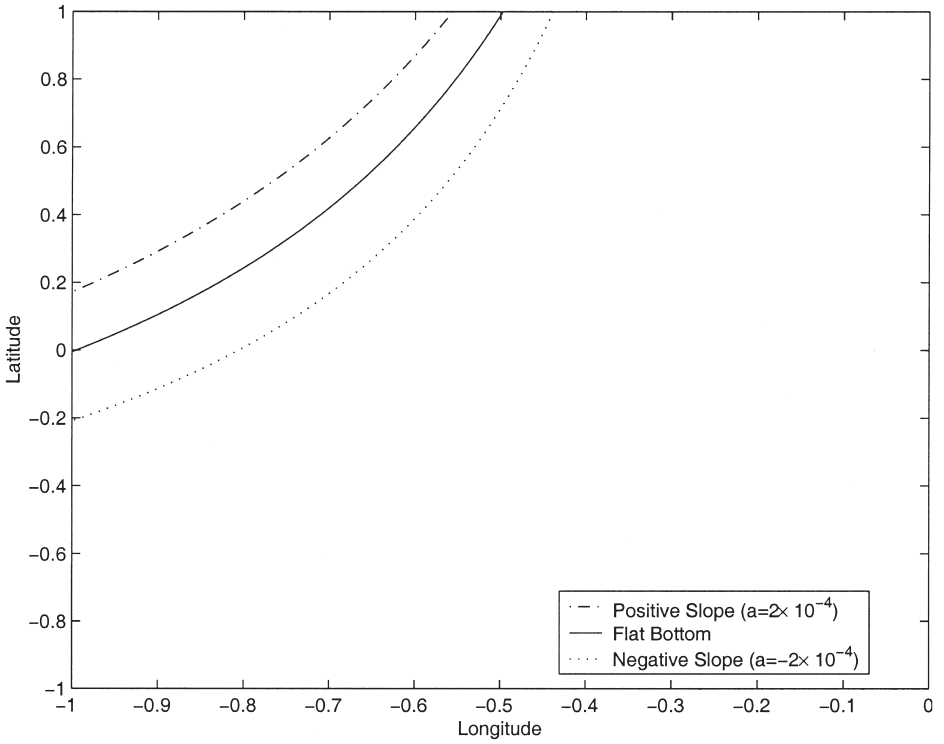

Figure 4. Plot of separatrices with the bottom slope a as a parameter.

case when $a < 0$. Recall, that the point R migrates westward with increasing positive a, showing that the recirculating gyre is gradually "squeezed out" of the domain. This statement is confirmed by examining the impact of topography on the separatrix which defines the interior boundary between the recirculating gyre, strongly controlled by cooling, and the interior mainly wind-driven circulation. The separatrix is given by

$$\phi(x, y) = \phi(0, l), \tag{46}$$

and in the case of linearly sloping topography (46) becomes

$$x = -\frac{\beta g' H_1 l^2}{f_0^2 w_0 (y + l)} \left(a + \frac{\beta}{f_0} (H_0 - ay) \right) \left[1 + \frac{H_1}{a(l - y)} \ln \left(\frac{\dfrac{f_0 a}{\beta} + H_0 - al}{\dfrac{f_0 a}{\beta} + H_0 - ay} \right) \right]. \tag{47}$$

A plot of the separatrix for various values of a is shown in Figure 4. When $a > 0$, and increasing, the separatrix shrinks toward the northwest corner of the domain, and vice verse for the case when $a < 0$.

Figure 5 shows three plots of η for various bottom slopes. In all plots, the interfacial

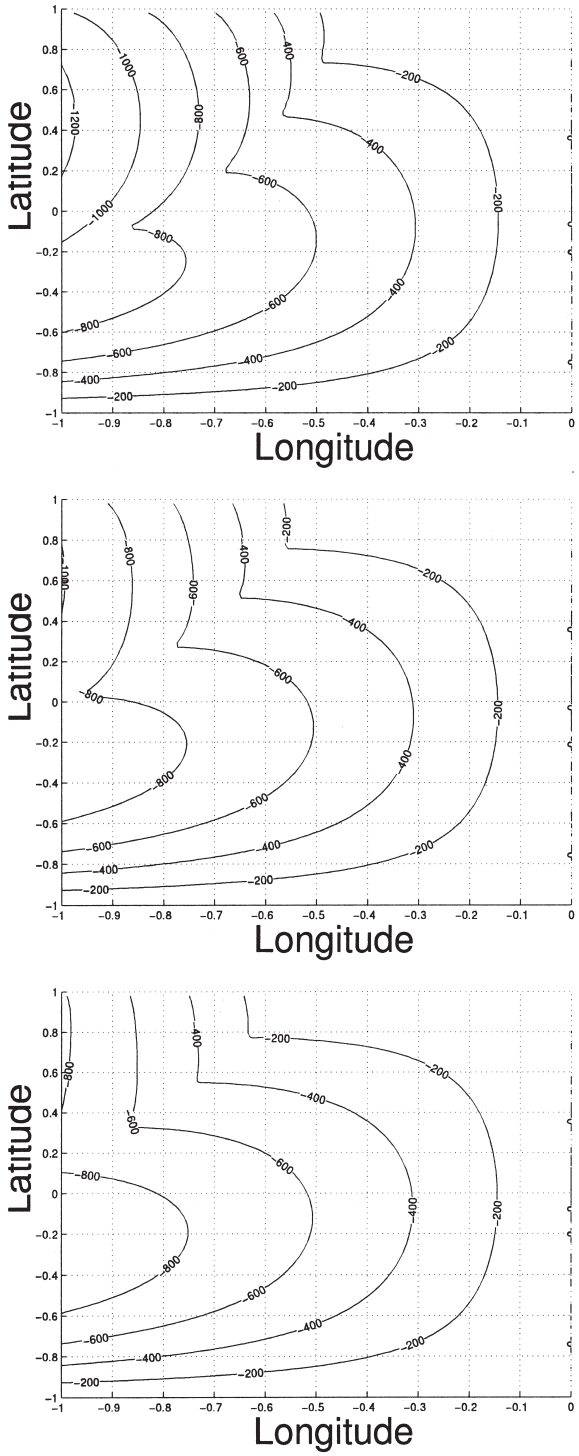

Figure 5. Contour plots of interfacial displacement η for 2-layer model; (a) total ocean depth deepens to the north ($a = -2 \times 10^{-4}$); (b) no topography present; (c) ocean shoals to the north ($a = 2 \times 10^{-4}$).

displacement at the eastern boundary depth is taken as $\eta^e = 0$, which means that the eastern boundary is in thermal equilibrium and no heating or cooling takes place there. Therefore, over the entire domain we see that there is cooling, and in the recirculating gyre region it is significantly enhanced. This is as we expected from our examination of the path of a water parcel, as the northwestern region is, therefore, a region of minimum PV. If we examine pressure contours in the domain, (Fig. 6), general features of the circulation are revealed. Firstly, in the upper layer the flow outside the northwestern region is nearly identical to the purely wind-driven gyre, which is as we might expect because the buoyancy flux across the layer interface has little effect in this region. In the northwestern region the general direction of flow is anticyclonic as would be suggested by the structure of the wind stress. However, the structure of the circulation patterns is governed by several parameters including the strength of the buoyancy flux, wind forcing and topography. Also as noted previously, the upper layer depth is always deeper than the reference equilibrium depth, that is $\eta < 0$ for the whole domain. This means that the water is being exchanged to the lower layer across the whole domain, but in large quantities in the northwestern region. In the lower layer any significant flow is almost entirely restricted to the northwestern region. Although some flow does occur outside of this region it is small due to the small quantities of water being transferred down into the lower layer. The important thing to note in the lower layer is that the flow in the northwestern region is cyclonic, as compared to the anticyclonic flow in the layer above. This lower layer flow is generated by the considerable interface displacement, cooling thus being important. Figure 7 shows how the parameter α changes the structure of the northwestern recirculating gyre region when there is no topography present. When $\alpha < 1$ a recirculation region exists, and as α decreases in magnitude the recirculation becomes more intense.

5. Results of the nonlinear 2-layer model

a. Location of recirculating gyre center and the Rossby repeller point

The quasi-geostrophic solutions in Section 4 reveal the qualitative impact of meridionally sloping topography on the recirculating gyre. In this section, the quasi-geostrophic approximation is relaxed. As a consequence we determine numerical solutions of (1) to (4). Before embarking on this approach, analytical results can be obtained for the positions of the gyre center and Rossby repeller point in the nonlinear case. To this end we first recast (9) in terms of the upper layer inverse planetary potential vorticity, namely

$$\left[-\Psi_y - \frac{\beta^2 g' h_1}{f^2 \mu} (H_0 - h_1 - \delta) - \frac{\beta g' \delta_y}{f\mu} h_1 - \frac{\beta g' \delta_{yy}}{2f\mu^2} (h_1^2 - (h_1^e)^2) \right] \left(\frac{h_1}{f} \right)_x + \Psi_x \left(\frac{h_1}{f} \right)_y = -w_e + q. \tag{48}$$

Numerical solutions of (48) are obtained by solving the three coupled characteristic equations (Ockendon *et al.,* 1999)

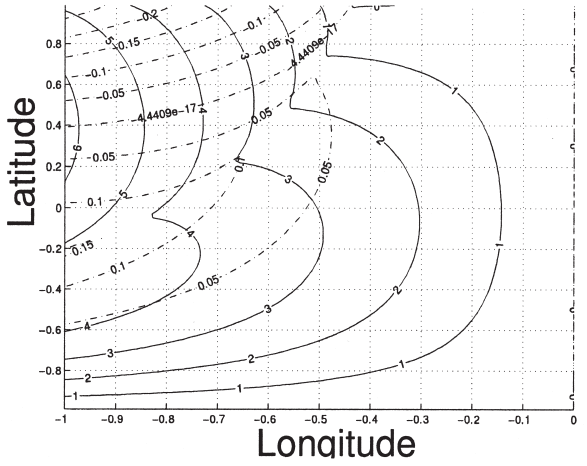

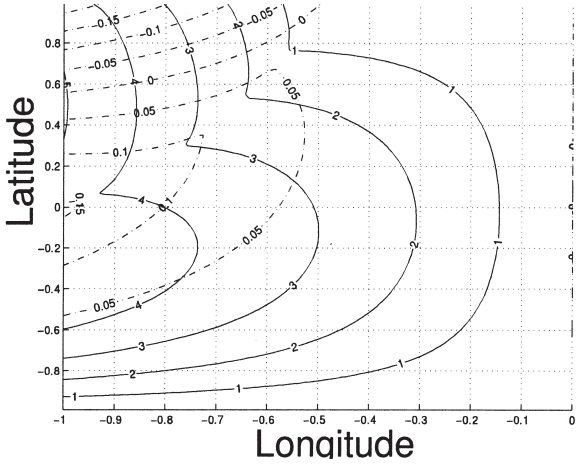

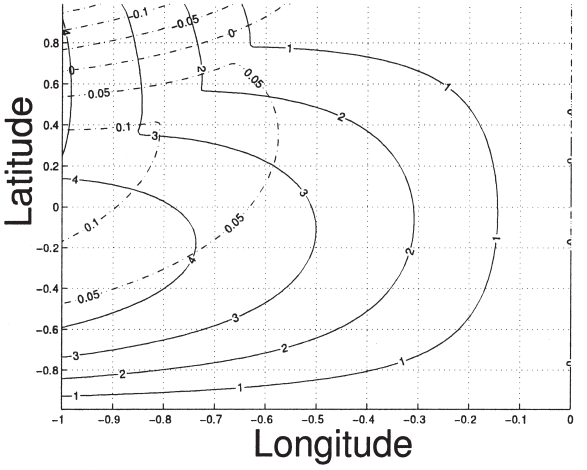

Figure 6. As in Figure 5, except contours of upper layer pressure (continuous line) and lower layer pressure (dotted line) are plotted.

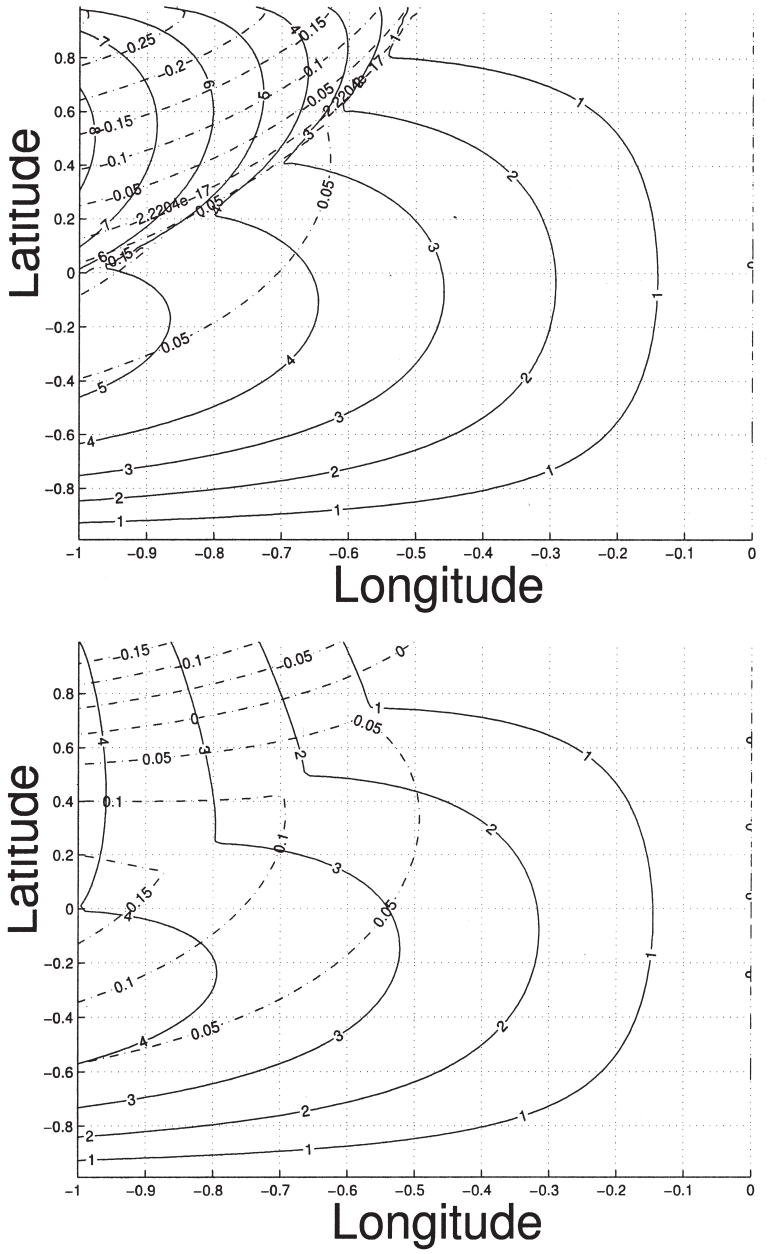

Figure 7. Contours of pressure with; (a) $\alpha = 0.46$; (b) $\alpha = 0.92$.

$$\frac{dx}{ds} = -\Psi_y - \frac{\beta^2 g' \chi}{\mu}\left(\frac{H_0}{f} - \chi - \frac{\delta}{f}\right) - \frac{\beta g' \delta_y}{\mu}\chi - \frac{\beta g' f \delta_{yy}}{2\mu^2}(\chi^2 - (\chi^e)^2), \tag{49a}$$

$$\frac{dy}{ds} = \Psi_x, \tag{49b}$$

$$\frac{d\chi}{ds} = -w_e + q, \tag{49c}$$

where $\chi = h_1/f$, is the inverse planetary potential vorticity in the upper layer and s is a parameter measured along the characteristics.

The location of C and R provide information about the area of the recirculating gyre. At R the depth-integrated wind-driven zonal velocity is balanced by the westward speed of long Rossby waves (see Fig. 2). Let the location of R be given by (x_R, l), where x_R is to be determined. At R the following equations are satisfied:

$$\frac{dx}{ds} = 0,$$

$$y = l.$$

The Rossby repeller point R is a stagnation point and the first equation is a statement of this fact. Using these conditions it is found that the zonal co-ordinate of the Rossby repeller point is given by

$$x_R = -\frac{\beta^2 g' l}{2f^3 w_0}\bar{h}(H_0 - \bar{h} - \delta) - \frac{\beta g' l \delta_y}{2f^2 w_0}\bar{h} - \frac{\beta g' l \delta_{yy}}{4f^2 \mu w_0}(\bar{h}^2 - (h_1^e)^2). \tag{50}$$

In the absence of topography (50) reduces to Eq. (39), provided f is replaced by f_0. In this case x_R in (50) is displaced to the east of the quasi-linear value in (39), for a given parameter regime. Further, the term proportional to δ_{yy} in (50) is absent in the quasi-linear expression for x_R, and it can have a significant impact on the value of the co-ordinate x_R. The term proportional to δ_{yy} in (50) is absent if the interfacial mass exchange is assumed to vanish at the eastern boundary (ie $\bar{h} = h_1^e$). We also observe that (50) is independent of k, a parameter whose value is highly uncertain. In other words, x_R is independent of the parameterization of the buoyancy flux.

The location of the recirculating gyre (see Fig. 2) center, C, can also be calculated analytically. Let C be located at $(-L, y_C)$, where y_C is to be determined. At C we require; (a) the zonal flow in the upper layer vanishes; (b) the potential vorticity attains an extremum. These conditions are equivalent to

$$\left.\begin{aligned} d\chi/dy &= 0 \\ p_{sy} &= 0 \end{aligned}\right\} \qquad \text{at } x = -L. \tag{51}$$

Using (8), the second of Eq. (51) yields

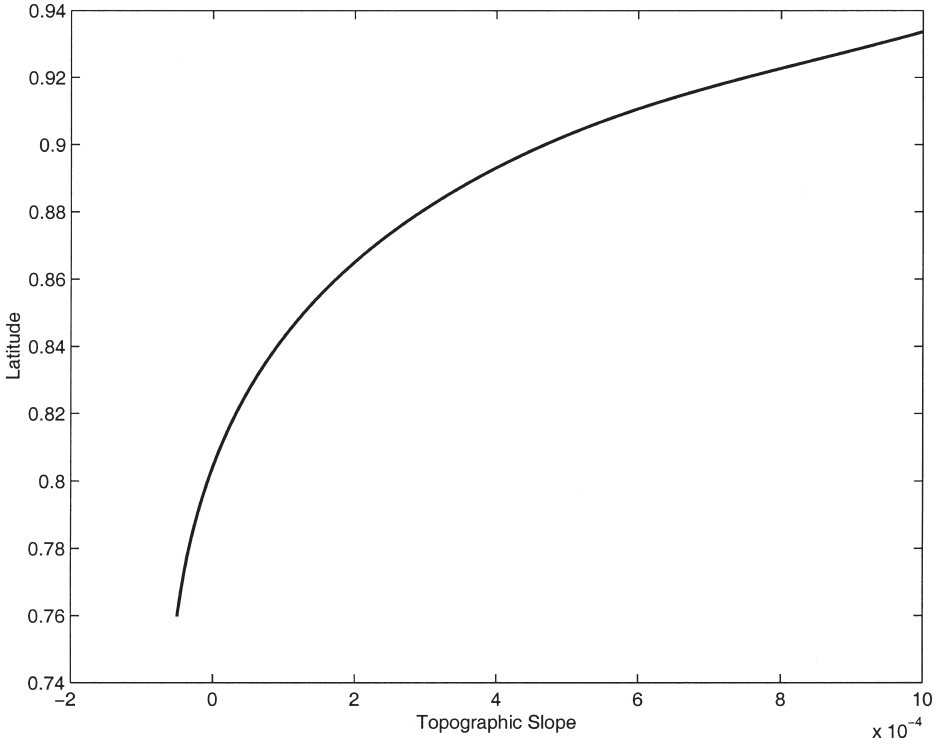

Figure 8. Plot of gyre center latitude against linear bottom slope.

$$-\Psi_y - \frac{\beta^2 g' h_1}{f^2 \mu}(H_0 - h_1 - \delta) - \frac{\beta g' \delta_y}{f\mu} h_1 - \frac{\beta g' \delta_{yy}}{2f\mu^2}(h_1^2 - (h_1^e)^2) = 0, \qquad \text{at } x = -L. \quad (52)$$

Note that (52) is the co-efficient of χ_x and that at $x = -L$ the left-hand side of (48) vanishes, using the first of Eq. (51). Therefore, at C we deduce that

$$h_1 = \frac{w_0}{k}\left(1 - \frac{y_c^2}{l^2}\right) + \bar{h}. \quad (53)$$

Substituting (53) into (52) yields a transcendental equation for, y_c, the latitude of C. This equation is given in Appendix A. If there is no topography, $\delta = 0$, then the gyre center is determined by the solution of a fourth order polynomial which is also derived in Appendix A. The latitude of C as a function of, a, the slope of the linear bottom topography $\delta(y) = ay$ is plotted in Figure 8. If the slope increases, $(a > 0)$, so that the ocean shoals to north, then the gyre center moves north, and vice versa if the ocean deepens to the north. By considering the size of the recirculating region as being set by a balance between the depth integrated wind forcing and the westward propagating long Rossby waves, this effect upon the gyre center would be expected. If the ocean shoals (deepens) to the north, the

topographic beta effect enhances (mitigates) the planetary beta effect, and the speed of long baroclinic Rossby waves is increased (decreased), thereby reducing (increasing) the size of the recirculating region moving the gyre center poleward (equatorward). Comparing the nonlinear result and the quasi-geostrophic results shown in Figure 3, it is seen that the results are qualitatively similar. However, the nonlinear results have a much smaller range of topographic slopes that allow a repeller point to exist.

b. Volume fluxes

Insight into the structure of the subtropical gyre circulation can also be obtained by considering the volume transport across the open zonal boundaries and the open meridional boundary to the west. In the absence of topography, the northern and southern zonal boundaries, where the Ekman pumping vanishes, by assumption, are streamlines for the depth integrated flow. Therefore, the downward Ekman pumping acting over the entire subtropical gyre is balanced by a discharge into the western boundary layer of the depth integrated flow. Is this statement valid when topography is present?

To answer this, first consider the meridional volume transport in the upper layer across the northern zonal boundary:

$$N_1 = \int_{-L}^{C(y)} v_1 h_1 dx \qquad \text{at } y = l. \tag{54}$$

Using (1) and (8), N_1 can be written as:

$$N_1 = \left[\frac{g'}{2f} (h^e + \bar{h}_1) - \frac{\beta g'}{3f^2 \mu} ((h^e)^2 + \bar{h}_1^2) \right] (h^e - \bar{h}_1) \tag{55}$$

where $h_1(C(y), y) = h^e$, a constant, and $h_1(-L, l) = \bar{h}_1$. For the sign of the term in the square brackets to be negative, μ must be positive and

$$3\beta(H_0 - \delta)(h^e + \bar{h}_1) + 3f\delta_y(h^e + \bar{h}_1) < 2\beta((h^e)^2 + \bar{h}_1^2) \qquad \text{at } y = l. \tag{56}$$

As the depth of the upper layer is constrained to be less than or equal to the total depth of the ocean, then for the term in the square brackets to be negative, there must be a substantial negative bottom slope. To obtain the bounds on δ_y, such that the term in the square brackets is negative, it is helpful to write

$$\delta_y = A(y) \frac{\beta}{f} (H_0 - \delta), \tag{57}$$

where $A(y)$ is an unknown function. Then μ takes the form

$$\mu = (A(y) + 1) \frac{\beta}{f} (H_0 - \delta). \tag{58}$$

On the northern boundary we obtain bounds for $A(l)$, and thus for $\delta_y(l)$, within which range the term in the square brackets in (55) is negative. The lower bound is given by $\mu > 0$, and yields, $A(l) > -1$. The upper bound can be deduced from (56), namely

$$A(l) = \frac{2[(h^e)^2 + \bar{h}_1^2]}{3(h^e + \bar{h}_1)(H_0 - \delta)} - 1, \tag{59}$$

where the first term on the right-hand side of (59) is strictly less than unity, since h^e, $\bar{h}_1 \leq H_0 - \delta$. Typically, $\delta_y(l)$ lies in the range $-0.965 \times 10^{-3} > \delta_y(l) > -1 \times 10^{-3}$.

Further insight on the volume flux across $y = l$ can be obtained by splitting the range of integration in (54) into two parts, from the eastern boundary to the Rossby repeller point, R, and from R to the oceanic edge of the western boundary current. We then obtain

$$\begin{aligned} N_1 = \left[\frac{g'}{2f}(h^e + \bar{h}) - \frac{\beta g'}{3f^2\mu}((h^e)^2 + \bar{h}^2)\right](h^e - \bar{h}) \\ + \left[\frac{g'}{2f}(\bar{h} + \bar{h}_1) - \frac{\beta g'}{3f^2\mu}(\bar{h}^2 + \bar{h}_1^2)\right](\bar{h} - \bar{h}_1). \end{aligned} \tag{60}$$

It is clear that if the eastern boundary condition is $h^e = \bar{h}$, as is assumed in this paper, then there is no volume flux in the upper layer through the northern boundary between the eastern boundary and the Rossby repeller point R. It is also clear from (55) that if the upper layer is deeper on the eastern (western) boundary than the western (eastern) boundary then the net volume flux in the upper layer is out of (in to) the domain, providing δ_y is outside of the bounds set above, else the opposite is true.

The volume flux through the northern boundary in the lower layer is given by

$$N_2 = \int_{-L}^{C(y)} v_2 h_2 dx \qquad \text{at } y = l, \tag{61}$$

and upon evaluation (61) becomes

$$N_2 = \frac{\beta g'}{f^2\mu}\left[\frac{((h^e)^2 + \bar{h}_1^2)}{3} - \frac{(H_0 - \delta)(h^e + \bar{h}_1)}{2}\right](h^e - \bar{h}_1). \tag{62}$$

The second term in the square brackets is always larger than the first, since h^e and $\bar{h}_1$ are both less than or equal to $H_0 - \delta$. Therefore the direction of the mass flux through the northern boundary in the lower layer is given by the sign of $(h^e - \bar{h}_1)$, which means that in most cases the mass flux will be in the opposite direction to the upper layer. The exceptions being when $\delta_y(l)$ is in the range of values stated above, meaning the sign of the term in the square bracket in (54) is negative.

The total flux through the northern boundary is given by

$$N_T = N_1 + N_2,$$

which upon using (55) and (62) becomes

$$N_T = \frac{g'\delta_y}{2f\mu}\left[(h^e)^2 - \bar{h}_1^2\right] \qquad \text{at } y = l. \tag{63}$$

We observe that the total mass flux is dependent upon the slope of the topography at $y = l$. For a flat bottom ocean there is no net mass flux through the northern boundary, as expected.

Following an analysis similar to that for the northern boundary, it can be shown that the meridional volume flux in the upper layer across the open southern zonal boundary, $y = -l$, is given by

$$S_1 = \left[\frac{g'}{2f}(h^e + \tilde{h}_1) - \frac{\beta g'}{3f^2\mu}((h^e)^2 + \tilde{h}_1^2)\right](h^e - \tilde{h}_1), \tag{64}$$

where $h^e = h_1(C(-l), -l)$ and $h_1(-L, -l) = \tilde{h}_1$. The meridional volume flux in the lower layer across $y = -l$ is given by

$$S_2 = \frac{\beta g'}{f^2\mu}\left[\frac{((h^e)^2 + \tilde{h}_1^2)}{3} - \frac{(H_0 - \delta)(h^e + \tilde{h}_1)}{2}\right](h^e - \tilde{h}_1), \tag{65}$$

and the total flux through the southern boundary is

$$S_T = \frac{g'\delta_y}{2f\mu}\left[(h^e)^2 - \tilde{h}_1^2\right]. \tag{66}$$

When the eastern boundary condition imposes no mass flux between the layers, $h_1^e = \bar{h}$ (the equilibrium depth), then there is no mass flux through the open zonal southern boundary, and there is no mass flux through the open zonal northern boundary between the eastern boundary and the Rossby repeller point, R. The inclusion of topography, in general, supports a flux through the open zonal boundaries that will not balance itself, that is the flux through the open northern zonal boundary is not equal in direction and magnitude to the volume flux through the open zonal southern boundary. Therefore, this flux must be balanced by a flux through the open meridional boundary.

Due to mathematical complexities, only the barotropic flux will be examined here. The total volume flux through the oceanic edge of the western boundary layer is given by

$$W = \int_{-l}^{l} (u_1 h_1 + u_2 h_2)\, dy \qquad \text{at } x = -L. \tag{67}$$

Evaluating (67) in a similar manner to the meridional volume fluxes across $y = \pm l$, yields

$$W = \left[\frac{g'\delta_y}{2f\mu}((h_1^e)^2 - h_1^2)\right]_{-l}^{l} - \int_{-l}^{l} \frac{\mu}{f}\Psi\, dy, \tag{68}$$

$$W = (N_T - S_T) - \text{Ekman}. \tag{69}$$

The total flux through the western boundary is clearly seen to be made up of two distinct parts. The first part is the topographically induced flux. This flux clearly balances the flux induced by the topography through the open zonal boundaries. The second part is independent of topography and represents the fluid injected by Ekman pumping over the entire domain. When the eastern boundary coincides with $x = 0$, the last term on the right-hand side of (69) is given by $(4w_0Ll)/3$.

c. Numerical solutions

The characteristic equations (49a, b, c) form a stiff system and is solved numerically using the Backward Differentiation Formulae (NAG, version 20, routine d02ejf) subject to no-normal flow on the eastern boundary. Explicitly the boundary conditions are

$$h_1(C(y), y) = h_1^e \text{ (a constant)}, \tag{70}$$

$$\frac{h_1(-L, y_1)}{f(y_1)} = \frac{h_1(-L, y_2)}{f(y_2)}, \tag{71}$$

where y_1 and y_2 are the start and end latitudes of a characteristic that begins and ends at the oceanic edge of the western boundary current.

The parameter values employed in the numerical solutions are found in Table 1. Two families of characteristic curves are required to span the domain. The first family begins at the eastern boundary and ends at the oceanic edge of the western boundary layer. The second family begins and ends at the oceanic edge of the western boundary layer. The separatrix that separates the two families of characteristics defines the "interior" boundary of the recirculation region in the northwestern corner (see Fig. 2). The separatrix meets the open northern boundary at the Rossby repeller point, R. Figure 9(a) shows contours of the upper layer depth when topography is absent. The northwestern corner can clearly be seen to be an area of maximum upper layer depth and therefore an area of minimum upper layer planetary potential vorticity. The recirculation region is characterized by a large interfacial mass flux, showing that the recirculation region is an area of maximum cooling. Figure 9(b) shows contours of the pressure in each layer, and are almost coincident with streamlines for the flow.[2] The recirculation region corresponds to an anticyclonic flow in the upper layer, and in the lower layer the flow is directed from the oceanic edge of the western boundary current to the northern zonal boundary. In the outer region the flow in the upper layer is nearly the wind driven solution and there is little flow in the lower layer.

With the introduction of a linear sloping bottom, $\delta(y) = ay$, the structure of the recirculating gyre is significantly altered when the ocean shoals to the north (Figs. 10(a) and (c)), corresponding to $a = 2 \times 10^{-4}$, the upper layer recirculating gyre in the

2. On an f-plane pressure is a streamfunction.

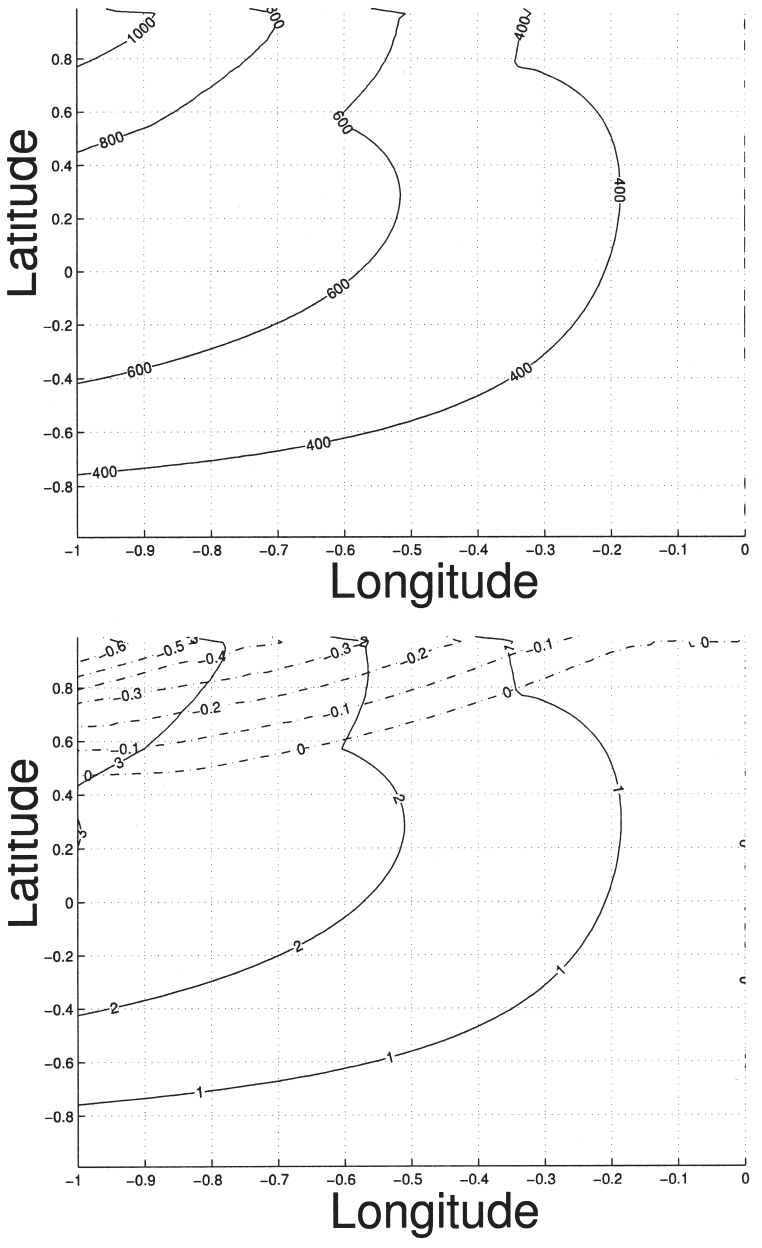

Figure 9. Contour plots of; (a) upper layer depth; (b) pressure in the upper layer, p_s, in continuous lines and pressure in the lower layer, $p_s + g'\eta$, in broken lines. Topography is absent.

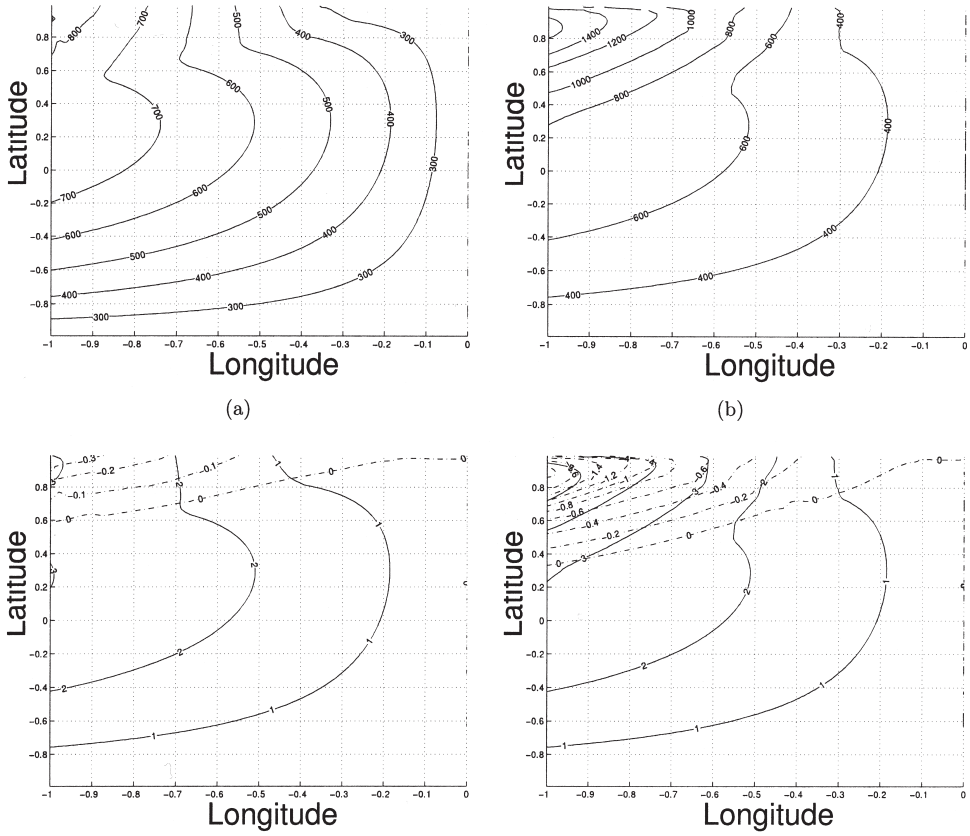

Figure 10. As in Figure 9, except topography $\delta(y) = ay$ is included with $a = 2 \times 10^{-4}$ (plots (a) and (c)) and $a = -2 \times 10^{-4}$ (plots (b) and (d)).

northwest corner shrinks in area, as predicted in Section 3a. In the lower layer the flow becomes more meridionally aligned in the recirculating gyre region, compared with the case when $\delta = 0$ (Fig. 9(b)). Contrast these solutions with those shown in Figures 10(b) and (d), in which $a = -2 \times 10^{-4}$, corresponding to an ocean that deepens to the north. The area of the recirculating gyre in the upper layer is increased. In this case, the flow in both layers in the northwest corner adopts a recirculating pattern.

We now consider the application of the model to the subtropical gyre of the North Atlantic. Specifically, the model is driven by Ekman pumping calculated using a fourth order interpolating polynomial fitted to the zonally averaged climatological zonal wind stress of Hellerman and Rosenstein (1983). Figure 11(a) shows a plot of the zonally averaged zonal wind stress over the latitude range 21N to 41N, together with the interpolating polynomial. The resulting Ekman pumping velocity vanishes at $y = -l$, l

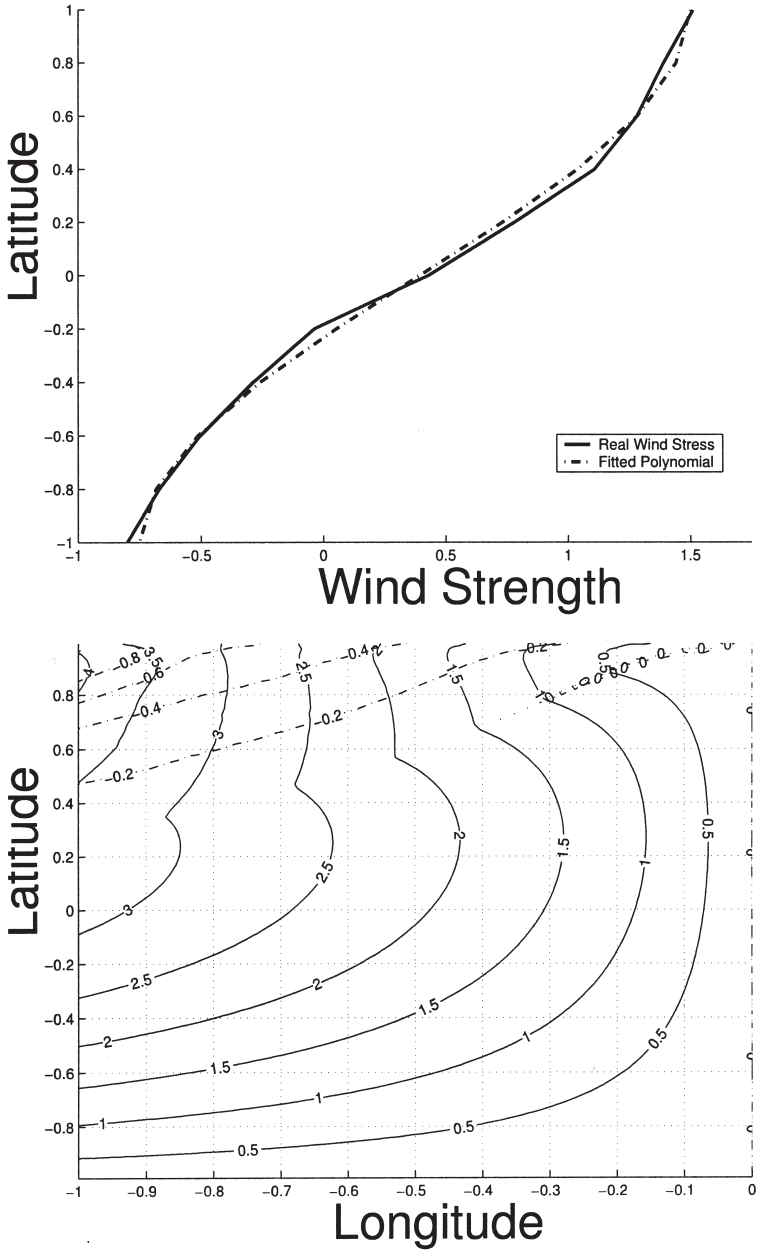

Figure 11. Plot of; (a) climatological Hellerman and Rosenstein (1983) wind stress against latitude; (b) contours of the upper and lower layer pressure field for a flat bottom ocean driven by Ekman pumping calculated using the wind stress in (a). The line types in (b) follow the convention of Figure 9.

(corresponding to latitudes 21N and 41N). Figure 11(b) shows a contour plot of the pressure field in each layer, associated with the climatological Ekman pumping, with topography absent. Comparing Figure 9(b) with Figure 11(b) we observe that the strength of the recirculating gyre is increased in the latter, in response to increased Ekman pumping in the northern half of the domain compared with the former case.

When topography and a representation of the eastern boundary are incorporated into the model, the resulting subtropical gyre circulation is shown in Figure 12(b). The GEBCO 97 topographic data set is used to calculate a zonally averaged bathymetry over the latitude range 24N and 27N, as shown in Figure 12(a). For computational purposes, solutions of (49a, b, c) are calculated using a fifth order interpolating polynomial representation of the zonally averaged bathymetry, plotted as a broken line in Figure 12(a). If instead the derivatives δ_y and δ_{yy} are calculated from the zonally averaged bathymetry curve, "noisy" fields, unsuitable for calculating numerical solutions of (49a, b, c), result. It is informative to compare Figure 12(b) with Figure 13(a) which shows contours of the upper 500 m in the Atlantic Ocean, as determined from a 0.5° eddy-resolving global ocean general circulation study by Semtner and Chervin (1992). Recalling that layer depth anomalies can be reinterpreted as temperature anomalies, we can see clear qualitative agreement between Figure 12(b) and Figure 13(a), particularly in the neighborhood of the recirculating gyre. The sharp reversals in the isotherms of Figure 13 are reproduced in this process model study, and the same overall structure, of a tight recirculation region in the northwestern corner surrounded by a broader recirculation is seen within the entire subtropical gyre of both figures. Figure 13(b), also taken from Semtner and Chervin (1992), shows contours of the surface heat flux, revealing that in the northwestern corner of the subtropical gyre in the North Atlantic, intense cooling takes place. In the layered model, this intense cooling region appears as a region of maximum upper layer depth.

6. Formulation of the 3-layer model

We now examine the impact of increased vertical resolution on the structure of the recirculating gyre. In particular we address the question, what is the horizontal extent of the recirculating gyre within each layer? To this end, we develop a 3-layer flat bottom planetary geostrophic ocean model in a domain identical to that discussed earlier. The introduction of topography into this 3-layer model greatly increases the mathematical complexity of the problem, and is beyond the scope of this study.

The equations of motion governing wind and buoyancy driven steady-state planetary geostrophic dynamics in a 3-layer ocean model are

$$\mathbf{k} \times \mathbf{u_1} = \frac{-1}{\rho_0 f} \nabla p_s, \tag{72}$$

$$\nabla \cdot (\mathbf{u_1} h_1) = -w_e + q_1, \tag{73}$$

$$\mathbf{k} \times \mathbf{u_2} = \frac{-1}{f} \nabla \left(\frac{1}{\rho_0} p_s + g'_1 \eta_1 \right), \tag{74}$$

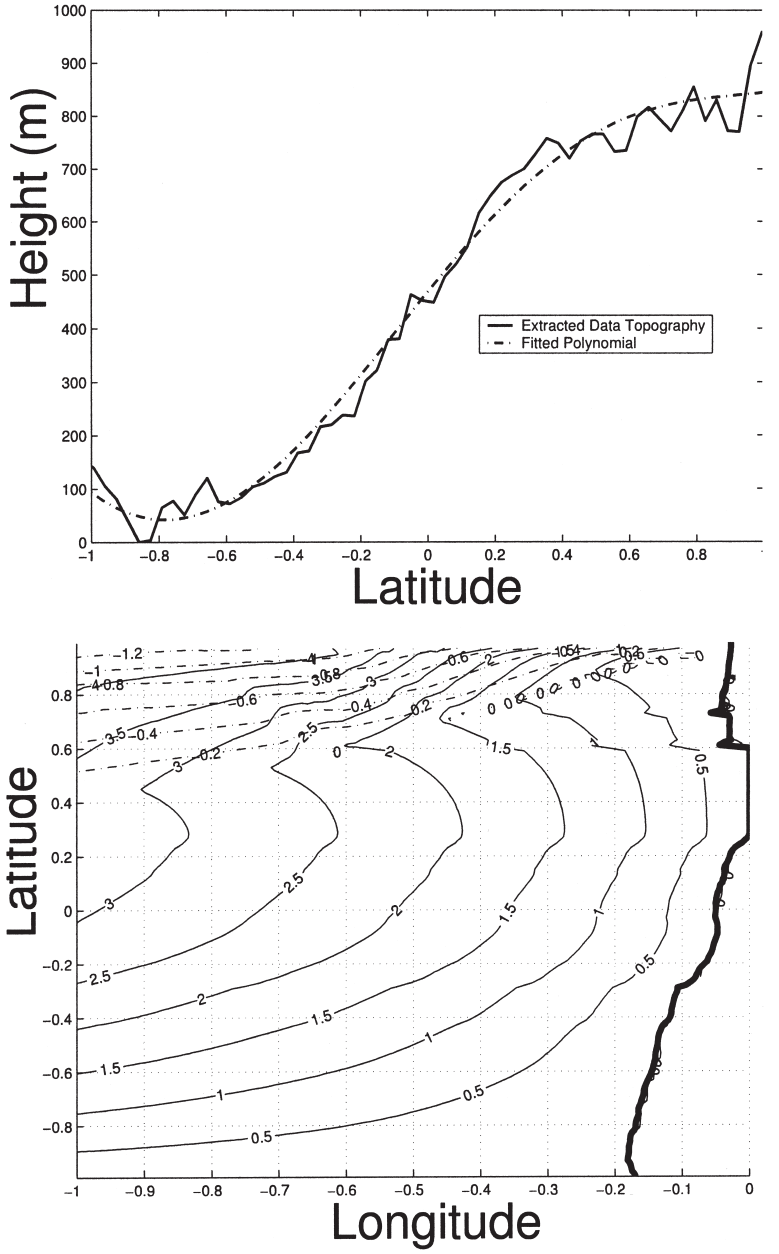

Figure 12. Plot of; (a) the zonally averaged topography (solid line) calculated from the GEBCO 97 data base for the latitude range 24N to 37N and an interpolating polynomial (broken line); (b) contours of the upper (solid line) and lower layer pressure fields when the model is driven by climatological Ekman pumping and includes representations of the topography and the eastern boundary.

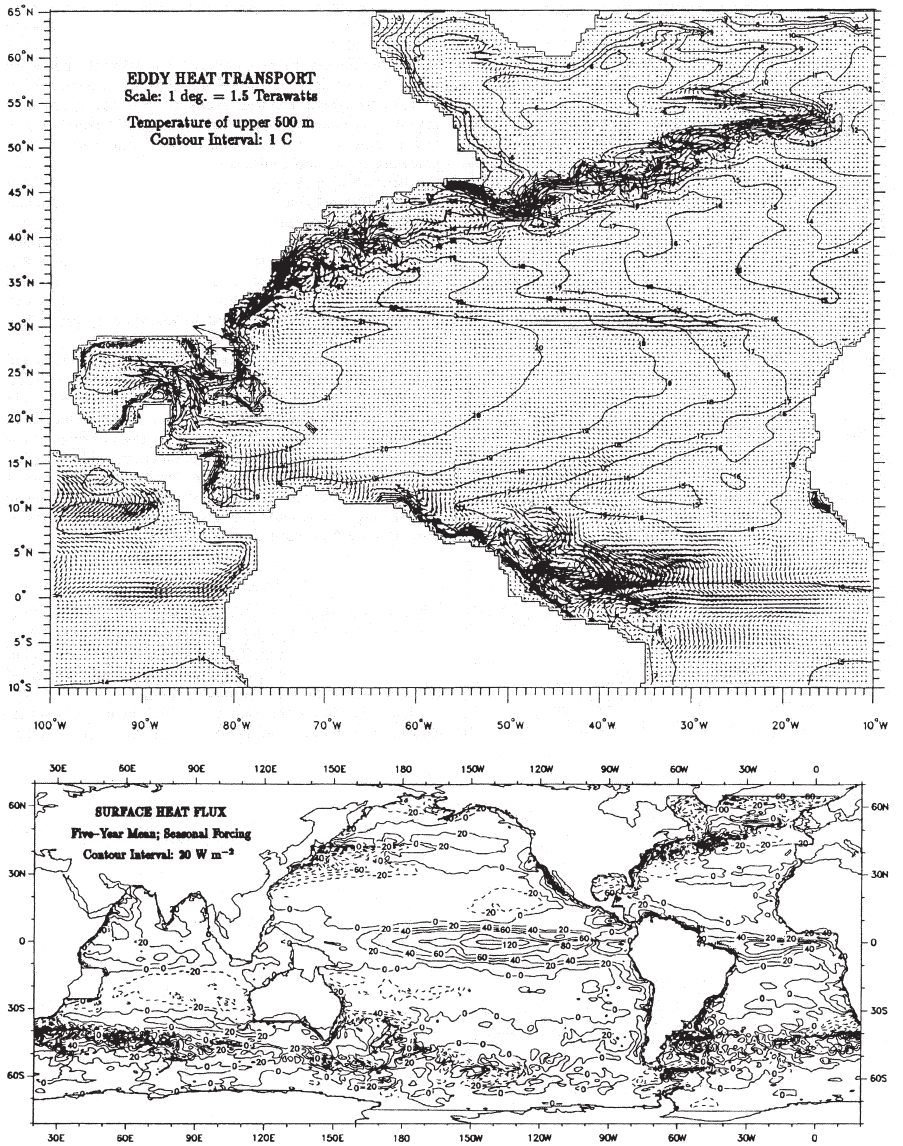

Figure 13. Plot reproduced from Semtner and Chervin (1992) of: (a) Contours of the time mean temperature averaged over the upper 500 m of the water column. Contour interval is 1°C. (b) Surface heat flux. Contour interval is 20 W m^{-2}.

$$\nabla \cdot (\mathbf{u_2} h_2) = -q_1 + q_2, \tag{75}$$

$$\mathbf{k} \times \mathbf{u_3} = \frac{-1}{f} \nabla\left(\frac{1}{\rho_0} p_s + g_1' \eta_1 + g_2' \eta_2\right), \tag{76}$$

$$\nabla \cdot (\mathbf{u_3} h_3) = -q_2, \tag{77}$$

where w_e is the Ekman pumping velocity, assumed to vary only with latitude, at the base of the Ekman layer, and q_1 and q_2 represent the fluid exchange between layers 1 and 2 and layers 2 and 3, respectively, due to surface heating and cooling. Following the notation of Section 2, $\mathbf{u_3}$ denotes the horizontal velocity in the bottom layer (labeled 3) and η_2 is the interfacial displacement between the middle layer 2 and the bottom layer 3.

It is straightforward to reduce (72) to (77) to a system of three equations that only involve the layer depths:

$$J\left(\frac{1}{\rho_0} p_s, \frac{h_1}{f}\right) = -w_e + q_1, \tag{78}$$

$$J\left(\frac{1}{\rho_0} p_s + g_1' \eta_1, \frac{h_2}{f}\right) = -q_1 + q_2, \tag{79}$$

$$J\left(\frac{1}{\rho_0} p_s + g_1' \eta_1 + g_2' \eta_2, \frac{h_3}{f}\right) = -q_2. \tag{80}$$

Upon adding (78) to (80) we obtain

$$\frac{1}{\rho_0} p_{sx} - \frac{g_1'}{H_0} h_{1x}(H_0 - h_1) + \frac{g_2'}{H_0} h_3 h_{3x} = \frac{f^2}{\beta H_0} w_e,$$

which upon integration with respect to x from the eastern boundary, gives

$$\frac{1}{\rho_0} p_s - \frac{g_1'}{2H_0} h_1(2H_0 - h_1) + \frac{g_2'}{2H_0} h_3^2 = \Psi + \Gamma, \tag{81}$$

where

$$\Psi(x, y) = \frac{-f^2}{\beta H_0} \int_x^0 w_e(s, y) ds,$$

$$\Gamma = \frac{1}{\rho_0} p_s^e - \frac{g_1'}{2H_0} h_1^e(2H_0 - h_1^e) + \frac{g_2'}{2H_0} (h_3^e)^2.$$

In the Sverdrup balance (81), variables with a superscript e denote the value of that quantity on the eastern boundary, $x = 0$. We now eliminate p_s in (78) and (80) using (81) to obtain a pair of coupled first order partial differential equations of the form

$$\left[\Psi_x - \frac{g_2'}{H_0} h_3 h_{3x}\right]\left(\frac{h_1}{f}\right)_y - \left[\Psi_y - \frac{g_2'}{H_0} h_3 h_{3y} + \frac{\beta g_1' h_1}{f H_0} h_1 (H_0 - h_1)\right]\left(\frac{h_1}{f}\right)_x = -w_e + q_1 \quad (82)$$

$$\left[\Psi_x - \frac{g_1'}{H_0} h_1 h_{1x}\right]\left(\frac{h_3}{f}\right)_y - \left[\Psi_y + \frac{\beta g_2'}{f H_0} h_3 (H_0 - h_3) - \frac{g_1'}{H_0} h_1 h_{1y}\right]\left(\frac{h_3}{f}\right)_x = -q_2 \quad (83)$$

Eqs. (82) and (83) represent the governing equations for the inverse planetary vorticity in layers 1 and 3, respectively. As in Section 2 we consider $w_e = -w_0(1 - y^2/l^2)$ and parameterize the mass exchange terms as $q_1 = -k_1(h_1 - H_1)$ and $q_2 = -k_2(h_1 + h_2 - H_1 - H_2)$, where k_1 and k_2 are constants. The choice of parameterization of the mass exchange between the lower two layers is open to endless debate. One could use the thickness of the middle layer in comparison to some reference depth, or as we have adopted here, the total depth of the upper two layers in comparison to some reference depth. We have chosen this parameterization for two reasons. First, we consider entrainment of fluid across any interface to arise from heating/cooling at the ocean surface. Thus it is reasonable to parameterize q_2 in terms of the departure of the total depth of the fluid, above the interface separating layers 2 and 3, from a reference value. Second, the parameterization allows analytical progress to be made in the quasi-geostrophic approximation. Adopting other parameterizations based on departures of the layer depths for q_2 will not, of course, introduce any new physics.

Calculating numerical solutions of (82) and (83) is beyond the scope of this paper. However, progress can be made by adopting the quasi-geostrophic approximation used for the 2-layer model in Section 2. In the linear quasi-geostrophic approximation, interfacial displacements are assumed to be small due to weak Ekman pumping. Let $h_1 = H_1 - \eta_1$, $h_3 = H_3 + \eta_2$ and assume that $(\beta y/f_0)$, (η_1/H_1), (η_2/H_3) are all small to the same degree. Linearization of the coupled system, (82) and (83) then yields

$$\left[\frac{\Psi_y}{f_0} + \frac{\beta g_1'}{f_0^2 H_0} H_1 (H_0 - H_1)\right]\eta_{1x} - \frac{\Psi_x}{f_0}\eta_{1y} + \frac{\beta g_2'}{f_0^2 H_0} H_1 H_3 \eta_{2x} = -w_e\left(1 - \frac{H_1}{H_0}\right) + k_1\eta_1 \quad (84)$$

$$\left[\frac{\Psi_y}{f_0} + \frac{\beta g_2'}{f_0^2 H_0} H_3 (H_0 - H_3)\right]\eta_{2x} - \frac{\Psi_x}{f_0}\eta_{2y} + \frac{\beta g_1'}{f_0^2 H_0} H_1 H_3 \eta_{1x} = -w_e \frac{H_3}{H_0} + k_2\eta_2 \quad (85)$$

while (81) becomes

$$\frac{1}{\rho_0} p_s - g_1'(H_1 - \eta_1) + \frac{g_1' H_1}{2H_0}(H_1 - 2\eta_1) + \frac{g_2' H_3}{2H_0}(H_3 + 2\eta_2) = \Psi + \Gamma, \quad (86)$$

where

$$\Psi(x, y) = \frac{-f_0^2}{\beta H_0}\int_x^0 w_e(s, y)ds$$

$$\Gamma = \frac{1}{\rho_0} p_s^e - g_1'(H_1 - \eta_1^e) + \frac{g_1' H_1}{2H_0}(H_1 - 2\eta_1^e) + \frac{g_2' H_3}{2H_0}(H_3 + 2\eta_2^e).$$

We have now reduced the problem to solving the linear coupled system of partial differential Eqs. (84) and (85). First we write (84) and (85) in the matrix form

$$\mathbf{A}\boldsymbol{\eta}_x + \mathbf{B}\boldsymbol{\eta}_y = \mathbf{c} \tag{87}$$

where

$$\mathbf{A} = \begin{bmatrix} \frac{\Psi_y}{f_0} + \frac{\beta g_1'}{f_0^2 H_0} H_1(H_0 - H_1) & \frac{\beta g_2' H_1 H_3}{f_0^2 H_0} \\ \frac{\beta g_1' H_1 H_3}{f_0^2 H_0} & \frac{\Psi_y}{f_0} + \frac{\beta g_2'}{f_0^2 H_0} H_3(H_0 - H_3) \end{bmatrix} \tag{88}$$

$$\mathbf{B} = \begin{bmatrix} -\frac{\Psi_x}{f_0} & 0 \\ 0 & -\frac{\Psi_x}{f_0} \end{bmatrix} \tag{89}$$

$$\mathbf{c} = \begin{bmatrix} -w_e\left(1 - \frac{H_1}{H_0}\right) + k_1\eta_1 \\ -w_e \frac{H_3}{H_0} + k_2\eta_2 \end{bmatrix} \tag{90}$$

and $\boldsymbol{\eta}^T = (\eta_1, \eta_2)$. The goal is to de-couple (87), thereby allowing analytical solutions to be determined. This can be achieved by first introducing new dependent variables $\boldsymbol{\xi} = (\xi_1, \xi_2)^T$ defined by

$$\boldsymbol{\eta} = \mathbf{P}\boldsymbol{\xi}, \tag{91}$$

where

$$\mathbf{P} = (\mathbf{p}_1, \mathbf{p}_2),$$

and $\mathbf{p}_1$ and $\mathbf{p}_2$ are the eigenvectors of $\mathbf{B}^{-1}\mathbf{A}$ written in column form. The eigenvectors and their corresponding eigenvalues are given in Appendix B. Using (91) it is straight forward to re-write (87) as

$$\boldsymbol{\Lambda}\boldsymbol{\xi}_x + \boldsymbol{\xi}_y = \mathbf{d}, \tag{92}$$

where

$$\boldsymbol{\Lambda} = \mathrm{diag}(\lambda_1, \lambda_2),$$

$$\mathbf{d} = \frac{1}{\nu_2 - \nu_1}\begin{bmatrix} \dfrac{\beta H_0}{f_0}\left(\nu_2 - \nu_2\dfrac{H_1}{H_0} - \dfrac{H_3}{H_0}\right) + \dfrac{f_0}{\Psi_x}\left[(k_2\nu_1 - k_1\nu_2)\xi_1 + (k_2 - k_1)\nu_2\xi_2\right] \\ -\dfrac{\beta H_0}{f_0}\left(\nu_1 - \nu_1\dfrac{H_1}{H_0} - \dfrac{H_3}{H_0}\right) + \dfrac{f_0}{\Psi_x}\left[(k_1 - k_2)\xi_1 + (k_1\nu_1 - k_2\nu_2)\xi_2\right] \end{bmatrix}$$

and

$$\nu_{1,2} = \frac{1}{2g_2'H_1H_3}\left[g_2'H_3(H_0 - H_3) - g_1'H_1(H_0 - H_1) \pm \mu^{1/2}\right].$$

In (92) coupling between the equations for ξ_1 and ξ_2 only arises from $\mathbf{d}$. However, if we assume $k_1 = k_2 = k$, say, we observe that (92) decouple. The assumption $k_1 = k_2$ is not overly restrictive, in the light of the highly idealized parameterization for the mass exchange terms q_1, q_2. Indeed, there is no *a priori* reason to expect that these constants of proportionality should be distinct. To summarize, when $k_1 = k_2 = k$, we find that ξ_1 and ξ_2 satisfy

$$\left[-\frac{\Psi_y}{f_0} - \frac{\beta}{2f_0^2H_0}\left[g_1'H_1(H_0 - H_1) + g_2'H_3(H_0 - H_3) + \mu^{1/2}\right]\right]\xi_{1x} + \frac{\Psi_x}{f_0}\xi_{1y} = \frac{w_e}{\nu_2 - \nu_1}\left(\nu_2 - \nu_2\frac{H_1}{H_0} - \frac{H_3}{H_0}\right) - k\xi_1, \tag{93}$$

$$\left[-\frac{\Psi_y}{f_0} - \frac{\beta}{2f_0^2H_0}\left[g_1'H_1(H_0 - H_1) + g_2'H_3(H_0 - H_3) - \mu^{1/2}\right]\right]\xi_{2x} + \frac{\Psi_x}{f_0}\xi_{2y} = -\frac{w_e}{\nu_2 - \nu_1}\left(\nu_1 - \nu_1\frac{H_1}{H_0} - \frac{H_3}{H_0}\right) - k\xi_2. \tag{94}$$

To solve for ξ_1 we rewrite (93) in the form

$$J(\phi_1, \xi_1) = \frac{w_e}{\nu_2 - \nu_1}\left(\nu_2 - \nu_2\frac{H_1}{H_0} - \frac{H_3}{H_0}\right) - k\xi_1, \tag{95}$$

where

$$\phi_1(x, y) = \frac{\Psi}{f_0} + \frac{\beta}{2f_0^2H_0}\left[g_1'H_1(H_0 - H_1) + g_2'H_3(H_0 - H_3) + \mu^{1/2}\right]y. \tag{96}$$

If we now consider $\xi_1 = \xi_1(y, \phi_1)$ then ξ_1 satisfies

$$\xi_{1y} + \frac{\beta H_0 k}{f_0 w_e}\xi_1 = \frac{\beta}{f_0(\nu_2 - \nu_1)}(\nu_2H_0 - \nu_2H_1 - H_3). \tag{97}$$

Clearly we wish to compare the solutions of the 2- and 3-layer models and therefore we again assume $k = K(1 + y/l)$. The solution of (97) is then given by

$$\xi_1(\phi_1, y) = \bar{\xi}_1(\phi_1)(l - y)^{-\alpha} - \frac{\beta H_0}{f_0(\alpha + 1)(\nu_2 - \nu_1)}\left(\nu_2 - \nu_2 \frac{H_1}{H_0} - \frac{H_3}{H_0}\right)(l - y), \quad (98)$$

where α is once again defined by (28). In common with the 2-layer model, the magnitude of α strongly controls the structure of the recirculating gyre.

A similar methodology leads to a solution for ξ_2 of the form

$$\xi_2(\phi_2, y) = \bar{\xi}_2(\phi_2)(l - y)^{-\alpha} + \frac{\beta H_0}{f_0(\alpha + 1)(\nu_2 - \nu_1)}\left(\nu_1 - \nu_1 \frac{H_1}{H_0} - \frac{H_3}{H_0}\right)(l - y), \quad (99)$$

where

$$\phi_2 = \frac{\Psi}{f_0} + \frac{\beta}{2f_0^2 H_0}[g_1' H_1(H_0 - H_1) + g_2' H_3(H_0 - H_3) - \mu^{1/2}]y. \quad (100)$$

To complete the solution for ξ_1 and ξ_2 we must determine $\bar{\xi}_1(\phi_1)$ and $\bar{\xi}_2(\phi_2)$. At the eastern boundary the condition of no normal flow must be imposed in all three layers. In layers 1 and 2 this boundary condition is equivalent to

$$\xi_1 = \frac{\eta_2^e - \nu_2 \eta_1^e}{\nu_1 - \nu_2} \qquad \xi_2 = \frac{\nu_1 \eta_1^e - \eta_2^e}{\nu_1 - \nu_2} \qquad \text{at } x = 0 \quad (101)$$

where η_1^e and η_2^e are constants. Application of the first of (101), with the aid of (96), yields

$$\begin{aligned}\xi_1(x, y) = {} & \left(\frac{\eta_2^e - \nu_2 \eta_1^e}{\nu_1 - \nu_2}\right)\left[1 + \frac{f_0 w_0 x}{\beta^2 H_0 l^2 R_1^2}(l + y)\right]^{\alpha} \\ & - \frac{\beta H_0\left(\nu_2 - \nu_2 \dfrac{H_1}{H_0} - \dfrac{H_3}{H_0}\right)}{f_0(\alpha + 1)(\nu_2 - \nu_1)}(l - y)\left[1 - \left(1 + \frac{f_0 w_0 x}{\beta^2 H_0 l^2 R_1^2}(l + y)\right)^{\alpha+1}\right]\end{aligned} \quad (102)$$

where

$$R_1^2 = \frac{1}{2f_0^2 H_0}[g_1' H_1(H_0 - H_1) + g_2' H_3(H_0 - H_3) + \mu^{1/2}]$$

and μ is a constant given by (114). Solution (102) is valid when $\phi_1 \leq \beta l R_1^2$, where the curve $\phi_1 = \beta l R_1^2$ is the separatrix between the two families of characteristic curves of (93).

Similarly, application of the second of (101) yields

$$\begin{aligned}\xi_2(x, y) = {} & \left(\frac{\nu_1 \eta_1^e - \eta_2^e}{\nu_1 - \nu_2}\right)\left[1 + \frac{f_0 w_0 x}{\beta^2 H_0 l^2 R_2^2}(l + y)\right]^{\alpha} \\ & - \frac{\beta H_0\left(\nu_1 - \nu_1 \dfrac{H_1}{H_0} - \dfrac{H_3}{H_0}\right)}{f_0(\alpha + 1)(\nu_2 - \nu_1)}(l - y)\left[1 - \left(1 + \frac{f_0 w_0 x}{\beta^2 H_0 l^2 R_2^2}(l + y)\right)^{\alpha+1}\right]\end{aligned} \quad (103)$$

where

$$R_2^2 = \frac{1}{2f_0^2 H_0}\left[g_1' H_1(H_0 - H_1) + g_2' H_3(H_0 - H_3) - \mu^{1/2}\right].$$

Solution (103) is valid when $\phi_2 \leq \beta l R_2^2$, where the curve $\phi_2 = \beta l R_2^2$ defines the separatrix between the two families of characteristic curves of (94).

The solutions (102) and (103) are valid in the domain spanned by characteristics emanating from the eastern boundary. In the northwest recirculating gyre region, the characteristic curves begin and end along the oceanic edge of the western boundary current (at $x = -L$), in a manner analogous to the 2-layer model. To determine the solution in the region spanned by this family of characteristic curves we once again demand that the value of the potential vorticity at the start and end points of each characteristic be identical. In layers 1 and 2 this boundary condition is equivalent to

$$\xi_1(\phi_1(y_1)) - \xi_1(\phi_1(y_2)) = \frac{\beta}{f_0(\nu_1 - \nu_2)}(H_0 - \nu_2 H_1 - H_3)(y_2 - y_1), \tag{104}$$

$$\xi_2(\phi_2(y_1)) - \xi_2(\phi_2(y_2)) = \frac{\beta}{f_0(\nu_2 - \nu_1)}(H_0 - \nu_1 H_1 - H_3)(y_2 - y_1). \tag{105}$$

Using the fact that the characteristics of ξ_1 and ξ_2 are isopleths of ϕ_1 and ϕ_2 respectively, we find that

$$\bar{\xi}_1(\phi_1) = \frac{\beta H_0(y_2 - y_1)\left[\nu_2 - \alpha - 1 + \nu_2\alpha\dfrac{H_1}{H_0} + \alpha\dfrac{H_3}{H_0}\right]}{f_0(\alpha + 1)(\nu_2 - \nu_1)[(l - y_2)^\alpha - (l - y_1)^\alpha]}(l - y_1)(l - y_2), \tag{106}$$

and therefore within the recirculating gyre region (98) takes the form

$$\begin{aligned}\xi_1(x, y) = {} & \frac{\beta H_0(y_2 - y_1)\left[\nu_2 - \alpha - 1 + \nu_2\alpha\dfrac{H_1}{H_0} + \alpha\dfrac{H_3}{H_0}\right]}{f_0(\alpha + 1)(\nu_2 - \nu_1)[(l - y_2)^\alpha - (l - y_1)^\alpha]} \\ & \times\left[-\frac{x(l + y)}{L} - \frac{\beta^2 H_0 l^2 R_1^2}{f_0 w_0 L}\right]^\alpha - \frac{\beta H_0}{f_0(\alpha + 1)(\nu_2 - \nu_1)}\left(\nu_2 - \nu_2\frac{H_1}{H_0} - \frac{H_3}{H_0}\right)(l - y)\end{aligned} \tag{107}$$

where $y_1(\phi_1)$ and $y_2(\phi_1)$ are solutions to the equation $\phi_1 = f_0 w_0 L/\beta H_0(1 - y^2/l^2) + \beta R_1^2 y$. Similarly, the solution for ξ_2 is given by

$$\bar{\xi}_2(\phi_2) = \frac{\beta H_0(y_2 - y_1)\left[\alpha + 1 - \nu_1 - \nu_1\alpha\dfrac{H_1}{H_0} - \alpha\dfrac{H_3}{H_0}\right]}{f_0(\alpha + 1)(\nu_2 - \nu_1)[(l - y_2)^\alpha - (l - y_1)^\alpha]}(l - y_1)(l - y_2), \tag{108}$$

and using (99) we find that in the recirculation gyre region

$$\xi_2(x, y) = \frac{\beta H_0(y_2 - y_1)\left[\alpha + 1 - \nu_1 - \nu_1\alpha\,\frac{H_1}{H_0} - \alpha\,\frac{H_3}{H_0}\right]}{f_0(\alpha + 1)(\nu_2 - \nu_1)[(l - y_2)^\alpha - (l - y_1)^\alpha]} \times \left[-\frac{x(l + y)}{L} - \frac{\beta^2 H_0 l^2 R_2^2}{f_0 w_0 L}\right]^\alpha + \frac{\beta H_0}{f_0(\alpha + 1)(\nu_2 - \nu_1)}\left(\nu_1 - \nu_1\frac{H_1}{H_0} - \frac{H_3}{H_0}\right)(l - y), \tag{109}$$

where again $y_1(\phi_2)$ and $y_2(\phi_2)$ are solutions to the equivalent equation $\phi_2 = f_0 w_0 L/\beta H_0(1 - y^2/l^2) + \beta R_2^2 y$. Finally, the solutions for ξ_1 (namely (102) and (107)) and ξ_2 (namely (103) and (109)) can be used to reconstruct the interfaces η_1 and η_2 using (91).

7. 3-layer model results

It is clear that we would expect to find, in general, three distinct regions in each layer, each bounded by a separatrix. These separatrices are those associated with the characteristics of the equations for ξ_1 and ξ_2 and will be apparent in all three layers. The three distinct regions will, in general, support circulation patterns not found in the 2-layer flat bottom model. Table 1 lists the parameters used in all the results shown here, unless otherwise stated, with the addition of $H_3 = 3 \times 10^3$ m and $g_2' = 1 \times 10^{-3}$ m s^{-2}. Figure 14 plots contours of the interfacial displacements, η_1 and η_2. The two separatrices can be seen in Figure 14(a) and (b). From these plots we can deduce the direction of the interfacial mass fluxes. Figure 14(a) shows that the mass flux between layers 1 and 2 is everywhere into layer 2, though strongest in the northwestern corner. Thus the upper layer is everywhere cooling and the strongest cooling is in the northwestern corner, as expected. Figure 14(b) shows that, in general, fluid is downwelling from layer 2 to layer 3, although in the northern central region fluid is moving from layer 3 to layer 2 corresponding to the region where the middle layer depth is at its most shallow.

Figure 15 shows the pressure contours in each of the 3 layers. In the upper layer we see a similar picture to the 2-layer model, a tight recirculation gyre in the northwestern corner and outside of this a flow broadly similar to the purely wind driven solution. With small changes to k and g_1', the existence of the second separatrix in the upper layer becomes clear, in contrast to the case shown in Figure 15(a). Qualitatively the circulation in the upper layer remains the same for this particular Ekman pumping in all parameter regimes that are oceanographically relevant. The direction of flow is anticyclonic, and the mass exchange is everywhere down into the middle layer. In the middle layer the two separatrices are clearly visible and create three distinct circulation patterns. In the region exterior to the outer separatrix we find weak circulation, similar to that in the outer region of the lower layer in the 2-layer model. This is due to the small amount of mass exchange in this region. In the northwestern region we find a circulation similar to that of the upper layer, a tight recirculation region that is anticyclonic. In this region the mass exchange is again down into the lower layer. In the middle region, between the separatrices, we observe two opposing gyres, an anticyclonic gyre in the southwestern portion and a cyclonic gyre in

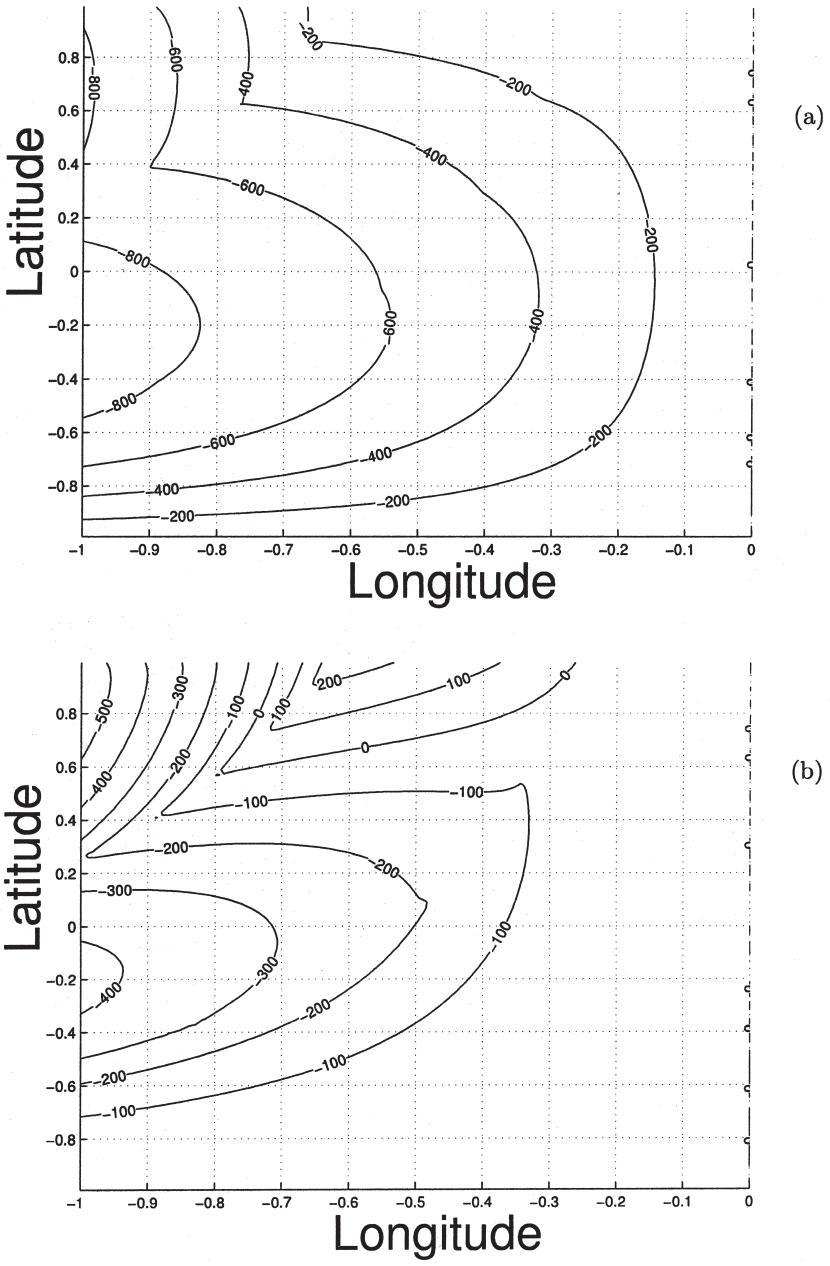

Figure 14. Contour plots of; (a) η_1 the interfacial displacement between layers 1 and 2; (b) η_2 the interfacial displacement between layers 2 and 3.

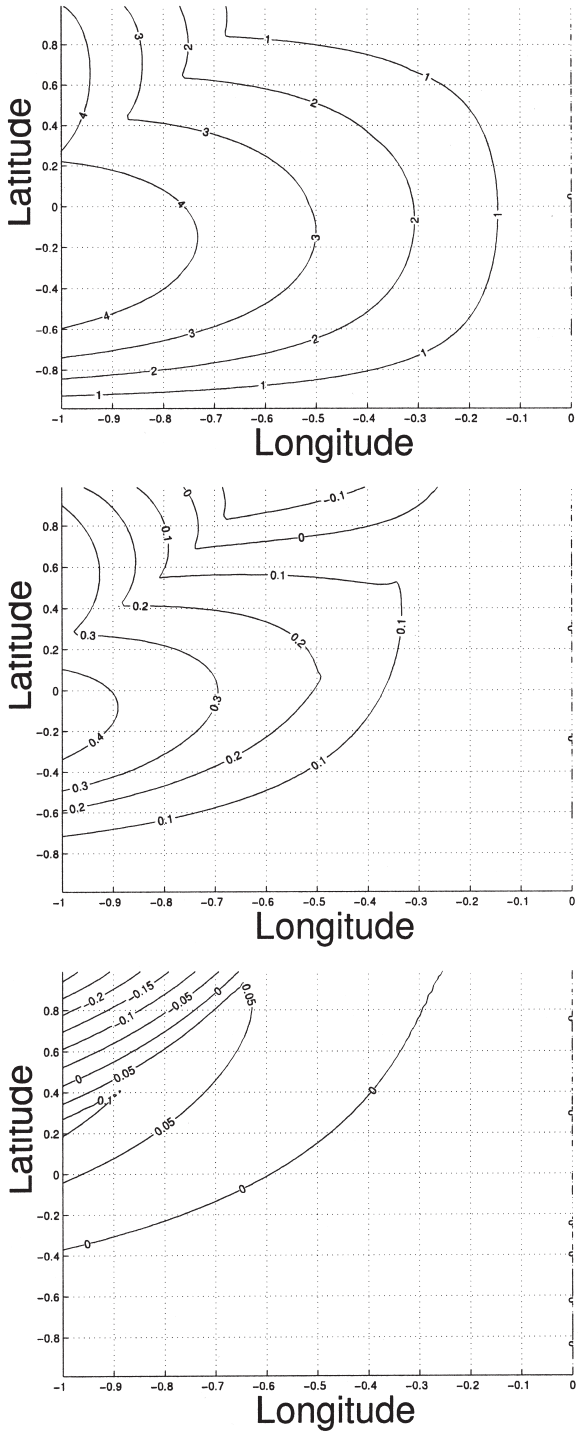

Figure 15. Contour plot of the pressure; (a) p_s, in layer 1; (b) $p_s + g'_1\eta_1$, in layer 2; (c) $p_s + g'_1\eta_1 + g'_2\eta_2$, in layer 3.

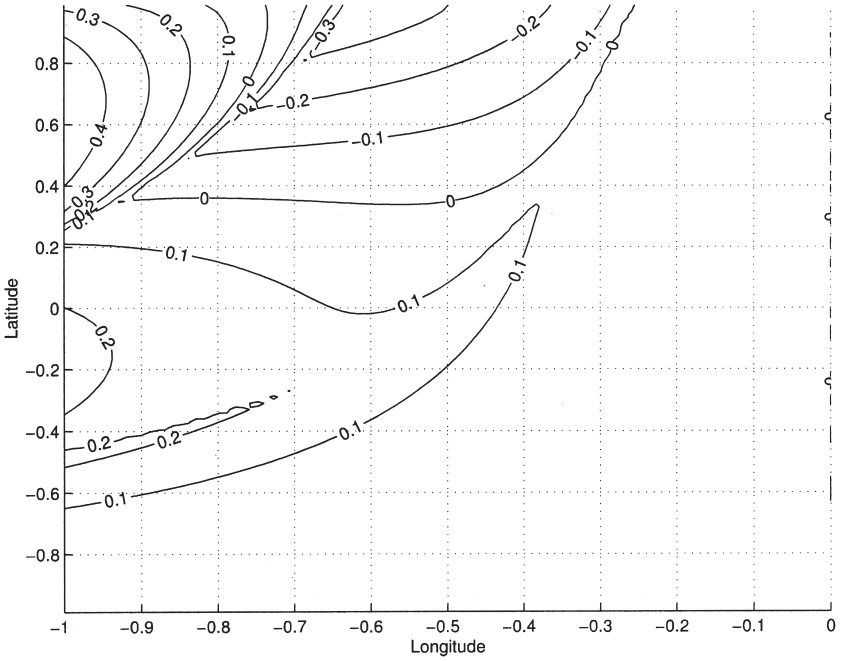

Figure 16. Contour plot of middle layer pressure when $K = 3 \times 10^{-10}$.

the northeastern portion. Generally, a cyclonic region which recirculates water through the northern boundary, and an anticyclonic region, which recirculates water through the western boundary, exist in varying strengths, depending upon the size of the parameter k. In the cyclonic region there is a net increase of mass. However, in the anticyclonic region the amount of mass exchange is enough to balance that received from the upper layer and indeed exceed it, although only by a small amount. This can be seen from the circulation in the lower layer (Fig. 15(c)). Here, as in the 2-layer model, there is only significant flow in the northwestern region. This circulation is cyclonic and indicates a net influx of fluid. The depth integrated flow however is equal to the purely wind driven barotropic flow and therefore the net flux through the northern boundary is zero. The sensitivity of the structure of the circulation in the middle layer to the distribution of the mass flux across the upper and lower interfaces is illustrated in Figure 16, where $k = 3 \times 10^{-10}$, a decrease in magnitude compared to the control value (see Table 1). The cyclonic region is much larger in extent compared with that in Figure 15(b).

8. Conclusions

Two- and three-layer linear quasi-geostrophic models and a two-layer nonlinear geostrophic model of the steady-state wind and buoyancy driven subtropical gyre circulation are developed in this paper, extending the study of CR. Buoyancy driving is represented by

mass exchange between the layers, parameterized in terms of the departure of a layer depth from an equilibrium value. CR demonstrated that models of this type support a recirculation region in the northwest corner of the domain, associated with a deep upper layer, where the upper layer planetary potential vorticity acquires a minimum and where significant cooling takes place. In the North Atlantic, this recirculation region is identified as the Sargasso Sea.

In this paper it is demonstrated that when the total ocean depth shoals (deepens) to the north the area of the recirculating gyre decreases (increases). This result is readily understood by studying the impact of topography on the separatrix, separating the two distinct families of characteristic curves spanning the entire subtropical gyre. At one end of the separatrix, where it intersects the northern open zonal boundary, is a stagnation point called the Rossby repeller (R). At this point the speed of long westward propagating baroclinic Rossby waves is equal and opposite to the zonal wind-driven depth integrated flow. The background potential vorticity gradient is modified by the presence of topography (via the topographic beta effect) thereby altering the speed of the baroclinic Rossby waves, and hence the location of R. The impact of topography on the location of the center of the recirculating gyre (C) is also determined analytically.

An analysis of the volume fluxes across the open boundaries, in the geostrophic 2-layer model, is also presented. The introduction of topography creates a flux through the open zonal boundaries which must in general be balanced by a flux through the open western boundary. The western boundary also has a constant flux determined by the amount of fluid injected by the Ekman pumping over the entire domain. If the eastern boundary condition implies no mass exchange between the layers at the boundary, then the flux through the zonal boundaries is confined to the northern zonal boundary west of the Rossby repeller.

The extension of this 2-layer model to include arbitrary topography is beyond the scope of this paper. From a technical viewpoint, it is not possible to analytically derive a generalized Sverdrup balance equation algebraically relating the layer depths. Without such an equation it is not possible to obtain a single equation for either the upper or lower layer potential vorticity. Thus, we are confronted with solving a coupled pair of first order partial differential equations, governing the potential vorticity in each layer.

Rather than attempt to find solutions of the planetary geostrophic equations, a numerical approach could be adopted to study the impact of arbitrary topography on the recirculating gyre. For example, a numerical model by Salmon (2002), of the wind driven 2-layer shallow water equations with arbitrary bottom topography, could provide some insight into this wind and buoyancy driven problem with arbitrary topography. The unsteady numerical model retains inertial terms and linear friction, thereby supporting a western boundary current, but does not include interfacial mass flux terms. However, the model is easily modified to include interfacial mass flux terms and this is being examined.

To address the impact of increased vertical resolution on the structure of the recirculating gyre, a 3-layer quasi-geostrophic model, with topography absent, is examined. Here we found that the circulation in the upper and lower layers is qualitatively similar to that in the

top and bottom layers, respectively, of a 2-layer model. Further, the recirculation region in the top layer of the 3-layer model responds in a similar manner to variation in the strength of the mass exchange between layers, as in the 2-layer case.

The middle layer has three distinct regions, associated with the existence of two separatrices. In the 3-layer model the circulation is governed by a pair of coupled first order partial differential equations governing the planetary potential vorticity in layers 1 and 3. The characteristic curves associated with each of these equations exhibit a separatrix and these subdivide each layer into three regions. In the interior region of the middle layer (ie the region between the eastern boundary and bounded to the west either by the edge of the western boundary current or the first separatrix encountered) the flow is weak due to weak buoyancy driving. In the northwest corner of this layer the flow is similar to that in the upper layer. However, in the region between the two separatrices the circulation can exhibit a rich structure, that is determined by the strength and distribution of the interfacial mass fluxes.

What features of the 2- and 3-layer solutions are exhibited in a continuously stratified ocean? A steady-state continuously stratified wind and buoyancy driven model for the subtropical gyre has been studied by Cushman-Roisin (1984). Here again, a recirculating region emerges, albeit for a rather narrow range of parameters. Analytical progress in the Cushman-Roisin (1984) study is made possible by the assumed similarity structure of the solution. However, the Cushman-Roisin (1984) solutions differ markedly with the layer solutions discussed here. The discrepancies between these two models are not surprising because the similarity structure imposes "self-similar solutions" at all levels, a property that is not exhibited in the 3-layer solutions. It would be interesting to numerically determine wind and buoyancy driven subtropical gyre solutions of the planetary geostrophic equations using the models of Edwards *et al.* (1998) or Samelson and Vallis (1997).

Finally, it would be worthwhile to determine how the extent of the recirculating gyre changes with unsteady Ekman pumping, varying on the seasonal time scale, say. The development of the unsteady model for long-time scales is straightforward (Johnson and Willmott, 1981) and the governing equation for the interfacial displacement is again a first order partial differential equation but now in three independent variables.

Acknowledgments. Ian Walkington gratefully acknowledges the support of a UK NERC research studentship while undertaking this research. This research was initiated when AJW visited CICESE, supported by research grant NER/B/S/2000/00016 from the UK NERC, to collaborate with the late Professor Pedro Ripa. We dedicate this paper to Professor Ripa. Finally, we thank Professor Benoit Cushman-Roisin for providing helpful advice and comments on this research.

APPENDIX

A. Recirculating gyre center latitude

Substituting (53) into (52) yields the transcendental equation for the gyre center latitude:

$$-2\beta(L+C)w_0\left(1-\frac{y_c^2}{l^2}\right)-fC_y w_0\left(1-\frac{y_c^2}{l^2}\right)+\frac{2f(L+C)w_0y_c}{l^2}+\frac{f(L+C)w_0\delta_{yy}}{\mu}\left(1-\frac{y_c^2}{l^2}\right)$$
$$-\frac{\beta^2 g'\bar{h}}{f^2}(H_0-\bar{h}-\delta)-\frac{\beta g'\delta_y}{f}\bar{h}-\frac{\beta g'\delta_{yy}}{2f\mu}(\bar{h}^2-(h_1^e)^2)-\frac{\beta^2 g' w_0}{kf^2}\left(1-\frac{y_c^2}{l^2}\right) \quad (110)$$
$$\times\left(H_0-\frac{w_0}{k}\left(1-\frac{y_c^2}{l^2}\right)-\delta\right)-\frac{\beta g' w_0\delta_y}{kf}\left(1-\frac{y_c^2}{l^2}\right)-\frac{\beta g'\delta_{yy}}{2f\mu}\left(\frac{w_0^2}{k^2}\left(\frac{1-y_c^2}{l^2}\right)^2-(h_1^e)^2\right)=0.$$

In the case when topography is absent, $\delta = 0$, and the eastern boundary corresponds to the meridional barrier $x = 0$ (i.e. $C(y) = 0$), (110) becomes

$$-2\beta L w_0\left(1-\frac{y_c^2}{l^2}\right)+\frac{2fLw_0y_c}{l^2}-\frac{\beta^2 g'\bar{h}}{f^2}(H_0-\bar{h})$$
$$-\frac{\beta^2 g' w_0}{kf^2}\left(1-\frac{y_c^2}{l^2}\right)\left(H_0-\frac{w_0}{k}\left(1-\frac{y_c^2}{l^2}\right)\right)=0. \quad (111)$$

Eq. (111) can be written as a fourth order polynomial for the gyre center latitude y_c:

$$\left(2\beta L w_0 f_0^2\epsilon^2+\frac{2f_0^3 L w_0\epsilon^3}{l}+\frac{\beta^2 g' w_0^2}{k^2}\right)\hat{y}^4+\left(4\beta L w_0 f_0\epsilon+\frac{6f_0^3 L w_0\epsilon^2}{l}\right)\hat{y}^3$$
$$+\left(2\beta L w_0 f_0^2(1-\epsilon^2)+\frac{6f_0^3 L w_0\epsilon}{l}-\frac{2\beta^2 g' w_0^2}{k^2}+\frac{\beta^2 g' w_0 H_0}{k}\right)\hat{y}^2$$
$$+\left(\frac{2f_0^3 L w_0}{l}-4\beta L w_0 f_0^2\epsilon\right)\hat{y}+\frac{\beta^2 g' w_0^2}{k^2}-2\beta L w_0 f_0^2-\beta^2 g'\bar{h}(H_0-\bar{h}) \quad (112)$$
$$-\frac{\beta^2 g' w_0 H_0}{k}=0,$$

where $\epsilon = \beta l/f_0$ and $\hat{y} = y_c/l$.

B. Eigenvalues and eigenvectors of $\mathbf{B^{-1}A}$

The eigenvalues, λ_1 and λ_2, satisfy the characteristic equation

$$det(\mathbf{B}^{-1}\mathbf{A}-\lambda\mathbf{I})=0.$$

After some lengthy algebra we obtain

$$\lambda_{1,2}=-\frac{\Psi_y}{\Psi_x}-\frac{\beta}{2f_0\Psi_x H_0}[g_1' H_1(H_0-H_1)+g_2' H_3(H_0-H_3)\pm\mu^{1/2}], \quad (113)$$

where

$$\mu = g_1'^2 H_1^2 (H_0 - H_1)^2 + g_2'^2 H_3^2 (H_0 - H_3)^2 + 2 g_1' g_2' H_1 H_3 \times (H_1 H_3 - H_0^2 + H_0 H_1 + H_0 H_3). \quad (114)$$

The eigenvector $\mathbf{p}_j$ associated with each eigenvalue λ_j ($j = 1, 2$) is given by

$$\mathbf{p}_1 = \begin{bmatrix} 1 \\ \dfrac{1}{2 g_2' H_1 H_3} [g_2' H_3 (H_0 - H_3) - g_1' H_1 (H_0 - H_1) + \mu^{1/2}] \end{bmatrix} \quad (115)$$

$$\mathbf{p}_2 = \begin{bmatrix} 1 \\ \dfrac{1}{2 g_2' H_1 H_3} [g_2' H_3 (H_0 - H_3) - g_1' H_1 (H_0 - H_1) - \mu^{1/2}] \end{bmatrix}. \quad (116)$$

REFERENCES

Chen, L. G. and W. K. Dewar. 1993. Intergyre communication in a three-layer model. J. Phys. Oceanogr., *23,* 855–878.

Cushman-Roisin, B. 1984. On the maintenance of the Subtropical Front and its associated countercurrent. J. Phys. Oceanogr., *14,* 1179–1190.

—— 1987. On the role of heat flux in the Gulf Stream-Sargasso Sea Subtropical Gyre System. J. Phys. Oceanogr., *17,* 2189–2202.

Edwards, N. R., A. J. Willmott and P. D. Killworth. 1998. On the role of topography and wind stress on the stability of the thermocline circulation. J. Phys. Oceanogr., *28,* 756–778.

Hautala, S. L. and S. C. Riser. 1989. A simple model of abyssal circulation, including effects of wind, buoyancy and topography. J. Phys. Oceanogr., *19,* 596–611.

Hellerman, S. and M. Rosenstein. 1983. Normal monthly wind stress over the World Ocean with error estimates. J. Phys. Oceanogr., *13,* 1093–1104.

Johnson, J. A. and A. J. Willmott. 1981. An unsteady wind-driven ocean circulation model. Dyn. Atmos. Oceans, *6,* 1–27.

Kawase, M. 1988. Establishment of deep ocean circulation driven by deep-water production. J. Phys. Oceanogr., *17,* 2294–2317.

Luyten, J. R. and H. Stommel. 1986. Gyres driven by combined wind and buoyancy flux. J. Phys. Oceanogr., *16,* 1551–1560.

Nishino, S. and S. Minobe. 2000. Buoyancy- and wind-driven circulation in an extended model of potential vorticity homogenization. J. Phys. Oceanogr., *30,* 2391–2403.

Ockendon, J., S. Howison, A. Lacey and A. Movchan. 1999. Applied Partial Differential Equations. Oxford University Press, 343 pp.

Rhines, P. B. and W. R. Young. 1982. Homogenization of potential vorticity in planetary gyres. J. Fluid. Mech., *122,* 347–367.

Salmon, R. 2002. Numerical solution of the two-layer shallow water equations with bottom topography. J. Mar. Res., *60,* 605–638.

Samelson, R. M. and G. K. Vallis. 1997. Large scale circulation with small diapycnal diffusion: The two-thermocline limit. J. Mar. Res., *55,* 223–275.

Scott, R. B. and A. J. Willmott. 2002. Steady-state frictional geostrophic circulation in a one-layer ocean model with thermodynamics. Dyn. Atmos. Oceans., *664,* 1–31.

Semtner, A. J. and R. M. Chervin. 1992. Ocean general circulation from a global eddy-resolving model. J. Geophys. Res., *97,* 5493–5550.

Spall, M. A. 2001. Large-scale circulations forced by localized mixing over a sloping bottom. J. Phys. Oceanogr., *31,* 2369–2384.

Veronis, G. 1988. Circulation driven by winds and surface cooling. J. Phys. Oceanogr., *18,* 1920–1932.

Willmott, A. J., N. R. Edwards and P. D. Killworth. 1996. Abyssal circulation in a circumpolar basin driven by discrete sources of buoyancy. J. Phys. Oceanogr., *26,* 49–64.

Wright, D. G. and A. J. Willmott. 1992. Buoyancy driven abyssal circulation in a circumpolar basin. J. Phys. Oceanogr., *22,* 139–154.

Received: *17 July, 2003;* revised: *15 March, 2004.*